Turbulences of the supersonic gas flow during cold spraying and their negative effects: A DNS CFD analysis coupled with experimental observation and laser impulse high-speed shadowgraphs of the particles in-flight flow

R.N. Raoelison, L.L Koithara, S. Costil, C. Langlade

Turbulences of the supersonic gas flow during cold spraying and their negative effects: a DNS CFD analysis coupled with experimental observation and laser impulse high-speed shadowgraphs of the particles in-flight flow.

R.N. Raoelison*, L.L Koithara, S. Costil, C. Langlade

Laboratoire Interdisciplinaire Carnot de Bourgogne - Site UTBM, UMR 6303 CNRS, Université de Bourgogne Franche-Comté UTBM, 90100 Belfort, France

* corresponding author: rija-nirina.raoelison@utbm.fr

Abstract

This paper investigates the phenomenological flow during cold spraying through DNS CFD analysis and experimental observations. The transient DNS computation shows that the gas flow begins to be instable inside the nozzle and generates self-sustained intermittent swirls across the nozzle exit due the shearing behavior of the flow. There is alternate swirling within the separated sheared layers on top and then on bottom of the jet, at sporadic time intervals. The swirls are not strictly periodic in nature, but they recur with an irregular frequency. The temperature field exhibits analogous variation and the thermal turbulence produces a heating confinement within the end zone of the nozzle, at the upper wall mostly. This phenomenon matches with the experimental erosion at the same zone due to a thermomechanical softening of the nozzle. The supersonic jet is self-oscillated along the flow direction and becomes more and more turbulent with a development of vorticity shedding at a certain distance from the nozzle exit. There is a transition from a rather stable jet towards a wake pattern that characterizes the vorticity regime. The thermal turbulence shows a development of turbulent plume which provides a clearer visualization of the straight jet and the abrupt transition into wakes. Experimental observations of particles motion ahead the nozzle exit confirm this turbulent behavior of the gas flow. High-speed shadowgraphy using nanoseconds pulsed laser spray illumination shows two regimes of particles kinematics, that is, a nearly straight jet prior to a progressive stream deviation, and then a full dispersion of the particles.

Such dispersion makes possible an oblique collision of the particles on the substrate whose negative effects highlighted in the literature are high porosity within the deposit, difficulty of coating formation, and substantial decrease in deposition efficiency. These findings provide further clarifications about how both gas flow and particles flow behave during cold spraying, and how deviation effects due to turbulences of the supersonic expansion may further alter the deposition capability of LPCS that already suffers from a low DE less than 40%.

Keywords: Cold spraying, CFD, turbulence, flow, in-flight behavior, shadowgraph

1. Introduction

Developed for years, the additive manufacturing (AM) is a technological breakthrough whose achievements and potentials are widely highlighted in both academic and industrial world with a growing dissemination. Since decades, a variance of AM method has been developed for metals, ceramics and their mixtures. By means of a supersonic gas flow, a ballistic deposition of these materials, in micron powder nature, onto a substrate enables for producing an additively manufactured component. The conventional methods, referred to as thermal spray process, use a supersonic gas flow that requires high temperature and high-pressure conditions. Working at low temperature and low pressure has recently extended the applicability of thermal spraying towards thermal sensitive materials while offering new opportunities viz. better materials performance, innovative material submicronic structuration, metallization of non-conductive surfaces, viable restoration or repair of metallic structures [1], and so forth as reported in some review papers [2–6].

At present, producing a supersonic flow condition is no longer a difficult task in thermal spraying and each developer succeeds in finding suitable settings for their own experiments. Regarding cold spraying, a broad range of successful processing conditions have been identified that falls into various categories of baseline working conditions and specific processing including deposition of nanotechnological components, composites-based structures and hybrid deposit/substrate combinations [7]. There is a substantial progress in terms of experimental achievements and the next milestone is to overcome the issue of weak deposition rate, particularly for low pressure cold spraying (LPCS). This includes a better understanding of the gas/solid flow and interaction during the supersonic deposition. Substantial works have been achieved but they are generally focused on the determination of the appropriate gas conditions for reaching the critical velocities of the particles to ensure a successful bonding onto the substrate, and thus a deposit formation. Experimental measures using laser system such as DPV2000, Laser-2-Focus or laser Particle Image Velocimetry are viable for that purpose [8].

An analytical approach based on an isentropic formulation of the gas flow is also widely used for a cost-effective assessment of deposition conditions over a large process data range [9–13]. The fluid dynamics simulation is exploited for a physically realistic depiction owing to its capability to compute the compressible flow that governs the global behavior of the cold spray

process. Through decades, those computational approaches resulted in a large characterization of cold spraying in terms of process parameters influences. Various effects such for gas conditions, particle features, nozzle features, powder feeding, and substrate conditions have been published. These analyses are generally focused on the in-flight behavior of the particles caused by their interactions with the gas stream. However, the phenomenological behavior of the gas flow is less investigated. The phenomena that govern the gas expansion have been progressively characterized. This paper addresses a brief review on this aspect to situate our study that focuses on the turbulent behavior of the supersonic gas flow and its detrimental effects during cold spray additive manufacturing.

2. Characterization of the supersonic gas flow during LPCS: a brief review

The phenomenological analysis of the gas flow during cold spraying has received attention in the literature. A few works are available, and they provide characterizations of the supersonic expansion by means of Schlieren photography. For capturing the flow, this system was the most efficient for a long period till to date. Shock waves are mainly revealed as physically observable phenomena of the supersonic flow since this high-speed optical technic is rather suitable for observing the density discontinuity within the flow. Clear descriptions of shock cells structures have been evidenced [14–18]. Visualization of fine details such as obliques shocks, incidence shocks, bow shock, compression waves, expansion wave and Mach disks led to a characterization of the gas flow into three major natures: the over-expanded flow, the under-expanded flow and the intermediate case denoted properly expanded flow that is an isentropic flow free of shock waves for which there is no abrupt discontinuity of gas temperature, density and velocity along the flow. Thus, the knowledges about the gas flow for LPCS also deal with the change in temperature, velocity and pressure during the gas expansion throughout the nozzle. The characteristics of LPCS as they are currently known are the isentropic or over- expanded nature of the flow depending on the gas nature and the gas setting. Typical experimental observations are provided in [14,16]. The computational analysis of the gas flow during LPCS mostly focus on the reproduction of these behaviors of the gas flow to assess the temperature and velocity of particles before they collide onto the substrate to form the deposit.

CFD simulations brought a further milestone in understanding the way these flow variants due to shock waves prevail as well as their effect on particle's in-flight behavior. Widely enacted

as investigative tool, the CFD RANS formulation is a good computational model for a physically realistic simulation of these shock waves phenomena outside the nozzle [14–17,19] while offering also a virtual visualization of internal shock waves (inside the nozzle) such as those appearing during low pressure cold spraying [14,19,20]. In this respect, the RANS computation is a cost-effective decision support tool to find conditions of properly expanded flow [19,20] which is believed to be the suitable situation for the particles to reach their best in-flight velocities. But the persuasive effects of shock waves are the abrupt variations of the gas temperature and velocity that affect the thermal behavior of particles rather than their in-flight velocity. Because of their micron size, the CS particles are prone to follow the instantaneous change in gas temperature whereas their kinematics are not significantly affected by the fast collapses of the gas velocity generated by the shock waves. The CS particles are small enough to overcome the gravity effect so that they conserve their kinetic energy produced by the supersonic velocity of the gas regardless the shock wave discontinuities. In the literature of cold spraying, this suggestion is widely supported by experimental measures of the particles velocity that concur with numerical simulation of the gas/particle interaction. Conclusive predictions of particles velocity have been largely produced.

However, the RANS simulation cannot compute the real turbulent behavior of the gas flow whose influence on particles kinematics has not been studied in a phenomenological view, especially for LCPS that is sensitive to deposition efficiency issues. The computation of averaged variation makes the RANS formulation inappropriate for investigating the real turbulent kinematics of the gas flow and its effects on the particle motions. Due to this limitation, we suggest a DNS computation to analyze the gas flow behavior and the phenomenological turbulences. The study focuses on LPCS that is the modern use of CS which greatly suffers from poor deposition rate, less than 40% generally, despite various explorative investigations [16,21–25]. The DNS CFD computation will be coupled with a laser high speed visualization of particles motion for a dual interest: to provide experimental observations of the phenomenological turbulence using the CS particles as tracers, and to characterize the kinematics of the particles due to this turbulence. Then, conclusions about deposition difficulties for LPCS will be depicted.

3. Computational model and experimental details

2.1 Phenomenological CFD model

The DNS CFD model computes the flow inside the nozzle and the free stream outside. The three-dimensional problem is simplified into a bi-dimensional geometry for an affordable simulation, but also to fit with the high-speed imaging observation. Thus, the simulation is focused on the cross section of the nozzle, that is, the vertical plane of symmetry of the real three-dimensional flow (Fig.1). The zone outside the nozzle is modelled by a computational media large enough to produce the external free flow within the atmospheric exit domain. The boundary conditions for this domain are defined by the ambient conditions of atmospheric pressure of 1atm and ambient temperature of 18°C. The gas inlet conditions are specified in terms of pressure and temperature which are set to the experimental pressurization conditions of the gas. The nozzle itself is assigned a wall temperature of 18°C and behaves as a motionless wall for the fluid flow. Since the particles are fed into the nozzle by a non-heated gas at ambient temperature, the boundary where the particles are injected is assigned a gas inlet condition of 1atm and 18°C. Indeed, the radial inflow of particles into the nozzle is due to a depressurization at the injection site where the pressure is lower than the outer atmospheric pressure.

The transient flow of the gas is described by the standard conservation equations of mass (Eq. 1), momentum (Eq. 2) and energy (Eq .3) solved by the density-based eulerian solver of Ansys Fluent. The gas density obeys to the ideal gas law. The gas is a newtonian fluid and its viscosity varies with temperature following the law of Sutherland. The energy equation uses the enthalpy formulation. We adopt the DNS approach for its suitability to compute the flow in a phenomenological way throughout the fluid domain. The computation utilizes a mesh size of 70µm in the domain of supersonic flow, a time increment of 10^{-6}s for a total duration of 10^{-3}s. This discretization is suitable to observe the space-time variation of the turbulences, but also makes the simulation affordable in terms of computational time and storage. This calculation was performed on the Cluster Lumière of “Mésocentre de Calcul de Franche-Comté” that has the capabilities of 8.4To Random-access memory, 2096 cores and 66.33 Tflops speed. Table 1 addresses the computational details for running the simulation of this study.

$$\frac{D\rho}{Dt} + \rho . div\left(\vec{V}\right) = 0 \qquad \text{(Eq. 1)}$$

$$\rho \frac{D\vec{V}}{Dt} = -\overrightarrow{\nabla p} + \mu \overrightarrow{\nabla . \underline{\underline{\tau'}}} \quad \text{with} \quad \underline{\underline{\tau'}} = \mu \left(\nabla \vec{V} + \nabla \vec{V}^T - \frac{3}{2} \nabla . \vec{V} \underline{\underline{I}} \right) \qquad \text{(Eq. 2)}$$

$$\rho C_p \frac{DT}{Dt} = \nabla . \left(\lambda \overrightarrow{\nabla T} \right) + \mu \underline{\underline{\tau'}} : \nabla \vec{V} \qquad \text{(Eq. 3)}$$

where the time derivative is the advective derivative formulation. ρ(kg/m^3), p (Pa), T(K) and $\vec{V}$(m/s) are the gas density, pressure, temperature and velocity. C_p(J/K.kg) is the calorific capacity and μ(kg/m.s) is the dynamic viscosity.

2.2 LPCS test and laser high-speed imaging observation

The experimental LPCS is performed using the portable system DYMET 423 fitted with a De Laval nozzle inside a compact spray gun. The powders are supplied by a vibrational powder feeder which is connected to the supersonic part of the nozzle via a radial injection. The steel nozzle has an axisymmetric section whose dimensions are specified in Fig.2. The powders feedstock is an in-house production manufactured by atomization of copper bulk sample. The copper powders are spherically shaped (Fig. 3) and sieved into suitable granulometry for successful kinematic temporal observations. Table 2 addresses granulometry details. They do match with the laser high-speed imaging system, capable of visualizing particles larger than 20µm in diameter, at speeds lower than 500m/s. The LPCS test uses a preheated and pressurized nitrogen (T_0=400°C, P_0=6bar).

The experimental visualization of the particles supersonic motion relies on a high-speed shadowgraphy that combines a pulsed backlight illumination with a high-resolution imaging. The micron sized particles are backlighted by a high illumination so that they generate a shadow, visualized by high-resolution imaging. The experimental configuration is shown on Fig. 4. The dynamic observation system consists of a strobe head providing a pulsed laser back intense illumination, and a high-speed CCD sensor head that captures video images of the particles shadow. The high-luminosity is produced by nanoseconds (40ns) pulsed diode laser. This intense light source is synchronized with the high-speed electronic shutter of the CCD sensor. Note that the LPCS is rather free of self-luminosity since the gas expansion occurs at low temperature outside the nozzle. There is also a synchronization of the strobe pulse and the CCD shutter with the video recording to capture a frame. The particles visualization is performed with a shutter time of 1µs. The rate frame is limited to 20 per second, that is, a

frame every 50ms. The CCD sensor has a pixel number of 1024 square, and a recorded image has a spatial resolution of 16µm/pixel.

3. Results and discussions

3.1 Indication of turbulent flow revealed by the DNS computation

The working pressure range in LPCS generally produces an over-expanded flow since the pressure drop during the expansion across the divergent part of the De-Laval nozzle falls below the atmospheric pressure. This specific feature of LPCS is known to involve shock waves inside the nozzle and ahead the exit due to the accommodation of the pressure. A series of shock waves occurs from the nozzle throat while the pressure self-adapts to reach the external atmospheric condition. This shock wave phenomenon is permanent as long as the ratio between the inlet pressure and the outer atmospheric pressure lasts, and it becomes a stationary phenomenon that can be visualized by an experimental static observation [14,16]. The steady state conservation equations of mass, momentum and energy using the RANS formulation has also provided further characterizations in terms of pressure, velocity and temperature variations throughout the nozzle. The shock waves generate a series of peaks that exhibits a periodic distribution with a regular variation until a progressive stabilization towards the ambient condition outside the nozzle (Fig. 5). However, such variations do not reflect the full behavior of the flow since they correspond to discontinuities due to the shock wave stagnation alone. Indeed, the variables behavior may also consist of irregular variations with random oscillations. These two typical behaviors are compared in Fig. 5 which evidences a RANS periodic and regular accommodation of the pressure against a DNS random fluctuation. Such difference is attributed to turbulences that are phenomenologically computed by the DNS method. The supersonic expansion throughout the nozzle induces a turbulent flow as shown by the strong fluctuation of velocity along the centerline (Fig. 6a). The abrupt variation across the nozzle exit towards outside also reveals significant turbulence of the free flow within the atmospheric media. There is a development of oscillations along the flow pattern (Fig. 6b). Both formation and effect of such turbulences are depicted in the next sections.

3.2 Flow oscillation and confined turbulence phenomena inside the nozzle

The oscillatory pattern of the flow (Fig. 6) is a major feature of the turbulence due to the supersonic expansion. The jet starts to get deformed inside the nozzle with a sharp transition

at the zone of particle feeding. Fig. 7a shows a symmetrical upstream flow and afterwards an onset of oscillatory pattern due to the inlet temperature and pressure of the secondary gas that are specified at the injection point. This inlet condition produces a continuous flow at lower temperature that deviates the confinement of velocity gradient from the bottom wall. Thereby, the supersonic flow leaves the divergent cone region while developing an asymmetrical shearing jet due to the asymmetrical confinement of velocity gradient on both upper and bottom part of the flow. The vorticity that results from this gradient clearly shows the formation and evolution of the sheared layers with a confinement at the upper wall and a deviation from wall at the bottom zone. Within the sheared layer, high rate of rotation (vorticity) magnitudes are reached (Fig. 7b), that indicates the fast-transient turbulence created by the shearing. The sheared layers also involve local rotational flows within the boundary layers and more significantly within the bottom zone due to the secondary gas inlet condition (Fig. 8). Therefore, the flow becomes instable with the evolution of this disturbance while the front flow propagates along the nozzle. During this propagation, the deviation of the sheared layers combined with the formation of rotational flow within the boundary layers along the nozzle wall generates an oscillatory pattern that guides the flow. The gradient of vorticity also gives a clear visualization of such deformation of the supersonic jet. The zones of high magnitude vorticity progress towards the nozzle exit with a persistent irregular development due to the random turbulence (Fig. 9). The supplementary video provides the time dependent visualization of the instable flow.

The flow oscillation develops a dissymmetrical shearing across the nozzle exit. A typical situation is shown in Fig. 9 where the vorticity zone is wider within the bottom part and then involves an upward deviation of the flow. The opposite side of the powder feeder inlet has a more uniform distribution of velocity and temperature (Fig. 10). Within the bottom region, the formation of an inward swirl (Fig. 11) drives a mass of fluid from the outer atmospheric zone to the inside bottom region at the nozzle exit. This re-entrant flow enables a local mixing of the flow with a low temperature flux from the nozzle exit that results in an abrupt decrease in temperature in this bottom region (Fig. 10a), and thereby the collapse the flow velocity (Fig. 10b) by dissipative effect due to the local increase of the thermo-dependent viscosity. The confined structure of the flow lasts through time but under a recurrent instable regime. Over the time, the jet moves up and down depending on the chaotic change of the flow ahead the

nozzle exit. Fig. 12 shows the temporal variation of temperature and velocity at the center of the nozzle exit and near both top and bottom wall. The centerline zone remains subjected to a high velocity flow with a smaller fluctuation compared to the variations within the confinement near the walls. The bottom wall region evolves at lower temperature with an amplitude variation close to that in the middle of the nozzle exit (Fig. 12a). The upper confinement yields the largest thermal fluctuation with a temperature level that oscillates between the value reached in the centerline zone and the value closed to the wall temperature boundary condition of 18°C. Since the thermal field governs the viscosity change, the velocity varies similarly to the thermal field (Fig. 12b).

Due to the repetitive peaks of temperature and velocity at the top region, the upper wall is subjected to more heating and rapid deterioration by thermomechanical softening. This zone can be sensitive to mechanical interactions with the particles jet that are locally exposed to high heating-up and high velocities. The heating of both particles and wall facilitates a sticking and then a clogging when those particles collide on the heated wall. Such circumstance was met during a LPCS deposition of fine copper powders (d50 = 8.808 µm) above a gas preheating temperature of 630 °C when working with a pressure of 6bar [21]. The consequence is a formation of an intermittent particles jet that causes a discontinuous particles flux [21]. In a few studies, further negative effects of the clogging phenomenon were depicted, such as poor coating quality due to high porosity, short operation times and nozzle replacement [26,27]. Recommendations to prevent the clogging consist in reducing the temperature of the nozzle inner wall from the outside by means of cold fluid cooling. A water cooling is an easily affordable solution, and a recycled refrigerated CO_2 enables significant efficiency [26,28]. However, the cooling solution cannot prevent another detrimental mechanical interaction between the particles and the nozzle wall that also impacts the longevity of the nozzle. The collision of the particles onto the nozzle wall promotes an erosion, especially in presence of hard particles. When using angular ceramic particles, the nozzle is rapidly damaged. The location of strong erosion is in accordance with the DNS analysis, that is, at the upper zone where the computation indicates the recurrence of high velocity peak due the turbulent flow (Fig. 12). The top wall gets more easily thinner over the whole surface of the inner wall which is also eroded by the particle's motions dragged by the self-sustained oscillation of the flow at the nozzle exit (Fig. 13). The thinning of the nozzle wall is highlighted on (Fig. 14).

3.3 Progression of instable flow outside the nozzle and particle dispersion

The free flow outside the nozzle exhibits two regimes: a shearing jet while leaving the nozzle and entering the atmospheric media, and then a strongly oscillatory regime. The parietal shearing jet evolves towards a continuous forced free shearing flow across the nozzle exit that results in a persistence of enfolding shear layers over a certain distance before an abrupt instability takes place. We can rely on the virtual visualization of the vorticity magnitude to identify these sheared layers and highly turbulent zone (Fig. 15a). The rotation rate values provide major features: the structure of the turbulence and the quickness of the rotational motion within those zones. Ahead the nozzle exit, the jet flow is nearly straight because of the continuously forced supersonic jet that comes from the nozzle. The confinement of high rotation rate at both side of the outward jet reveals that this confined zone develops permanent fast swirls which trigger the chaotic turbulence of the free flow. At the nozzle exit, the upstream instability also disturbs the downstream flow that generates onset of dissymmetrical vortices within the nearly straight jet. Instable swirls occur at the sheared layers region, on top and then on bottom and vice versa alternately at sporadic time intervals. The structure of the swirl changes from one moment to the next (Fig. 16). The swirls are not strictly periodic in nature, but they recur with an irregular frequency because of the chaotic nature of the turbulence. The peak repetitions plotted in Fig. 12 shows such pseudo-periodicity. As long as the nozzle is fed with supersonic flow, the intermittent swirls are self-sustained and therefore they alternately drive the free flow from the bottom upwards. The cycle is repeated over and over and changes the behavior of the jet into an oscillation induced flow with a self-sustained fluctuation. The thermal turbulence shows a clearer view of the jet behavior. The heat transfer produced by the convective motion along the flow direction evidences the nearly stable jet and its size ahead the nozzle exit prior to the development of turbulent plume where the flow starts oscillating. The time dependent behavior of the thermal turbulence can be visualized in the supplementary video.

The instability of the flow grows in the downstream direction with an abrupt change due to a development of a vorticity pattern (Fig. 17). A series of high vorticity core is alternately shed on top and bottom of the flow from the left to the right. The development of this phenomenon can be explained as the results of the continuous shearing force generated by the jet in the direction of the flow, combined with the self-sustained oscillations at the nozzle exit. In the

vorticity pattern, there is no development of vortex shedding albeit the wake revealed by the self-organization of the vorticity looks like a von Karman vortex street. At the vorticity cells, the flow is not governed by large vortices swirling. The local rotation is limited by the predominance of the axial velocity of the jet along the flow. Fig. 17 displays a typical ratio of axial and radial velocity of the flow along the centerline. The velocity component perpendicular to the axial direction of the flow varies from negative to positive value in a pseudo-periodic way but such variation does not locally exceed 50% the axial velocity. Therefore, the upward or downward lift force generated by the local rotation is less than the axial lift force of the jet, that results in a local deviation of the stream instead of a curling up tendency found in a real von Karman vortex street. The continuous shearing force of the jet produces thereby a series of deviation which also follows the mutual interaction with the self-sustained oscillations at the nozzle exit. The deviations are therefore generated from one side of the jet, and then from the opposite side, within the sheared zone of the flow so that permanent oscillations appear within the region of high vorticity and grow along the flow direction to create the instable turbulent wake.

The high-speed visualization of the powders flow at the nozzle exit corroborates the DNS computation of the supersonic flow of the expanding gas outside the nozzle. The behavior of the powders is similar as for the flow regimes of the gas. There is a zone of stable flow for the particles over a certain distance ahead the nozzle's exit (Fig. 18a) where the gas adopts the straight flow regime. The particle jet is also straightly shaped and the length of the stable zone for both particles and gas are comparable, in the same range of 25-30mm. The progression of the downstream oscillations of the gas flow is also experimentally revealed by the kinematics of the particles. Due to the deviation of the gas stream that prevails, the particle jet is no longer straight, and particles oblique path appears. The particles are deviated at both side of the particles jet which becomes progressively scattered as the distance from the nozzle exit increases (Fig. 18a,18b). The particles distribution gets more and more sparse with a strong dispersion within the zone of turbulent gas flow characterized by the instable turbulent wake (Fig. 18c-e). A clear transition of dispersion is observed at 150mm-165mm that corresponds to the onset of vorticity shedding whose magnitude distribution along the centerline is plotted in Fig. 19. The zone of high vorticity beyond 150mm specifies the vortex shedding. The particles dispersion in this instable zone changes the particles path before the collision. An

oblique deviation prevails, and the particles collide on the substrate at an oblique incident angle whereas the suitable deposition condition for optimizing the particles kinematics is a normal impact, that is, a collision perpendicular to the substrate. Oblique collision is found to generate high porosity within the deposit or to drastically decrease the deposition efficiency or even to prevent the coating formation when the collision angle (with respect to the normal to substrate surface) exceeds typical value of 60° [29,30]. Such deviation effects due to the turbulence of the flow further alter the deposition capability of LPCS that already suffers from a low DE lower than 40%. Note that the dispersion of the particles within the gas flow is also influenced by the Stokes number of each particle. The higher the Stokes number, the more the particle more deviate from the gas flow streamlines. Such event due to this role of the Stokes number is expected to occur due to both powder granulometry and supersonic flow velocity regime in cold spraying.

4. Conclusions

The phenomenological flow and negative effects of the expansion of supersonic gas during cold spraying are investigated using a DNS computation coupled with experimental observation including a visualization of particles jets by means of high-speed laser impulse shadowgraph.

- The supersonic flow is readily disturbed inside the nozzle at the zone of particles radial injection and remains instable during the flow progression.
- A development of oscillations along the flow pattern characterizes the phenomenological turbulence of the supersonic expansion.
- The self-sustained oscillations of the flow at the nozzle exit generates repetitive peaks of temperature and velocity near the nozzle wall. This parietal phenomenon, conducive to a thermomechanical softening, is corroborated by an experimental thinning of the nozzle wall by continuous erosion.
- The flow oscillation develops a dissymmetrical separated shear layers with a higher thermal and kinematic confinement at the upper nozzle wall region. This detrimental confinement agrees with the experimental observation of strong erosion within this region.
- At the nozzle exit, intermittent swirls are self-sustained and therefore they alternately drive the free flow from the bottom upwards. The cycle is repeated over and over that

changes the behavior of the jet into an oscillation induced flow with a self-sustained fluctuation.

- The instability of the flow grows in the downstream direction with an abrupt change due to a development of a vorticity pattern. A series of high vorticity core is alternately shed on top and bottom of the flow.
- The behavior of the powders visualized by the high-speed shadowgraph is similar as for the flow regimes of the gas, that is, a zone of nearly stable flow over a certain distance ahead the nozzle's exit and then a zone of dispersed flow due to the strong turbulence of the gas stream.
- Due to the particle dispersion, oblique deviation of particles paths and its negative effects prevail. Based on published studies, high porosity within the deposit, difficulty of coating formation, and substantial decrease in deposition efficiency are expected to occur.

Appendix

Temporal vorticity shedding outside the nozzle showing the temporal self-sustained oscillatory flow.

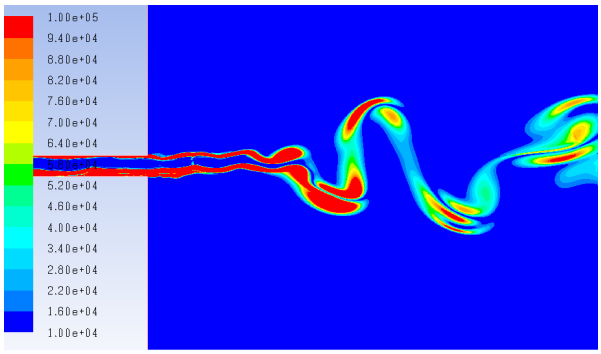

(0.005s)

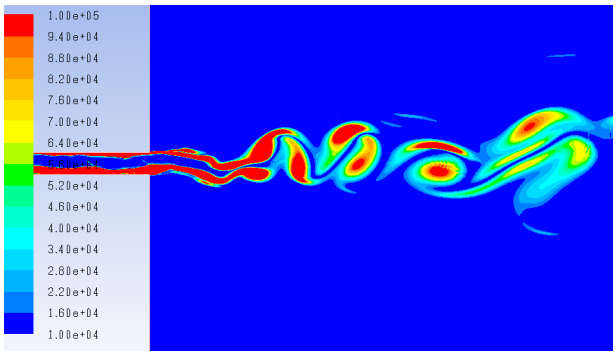

(0.01s)

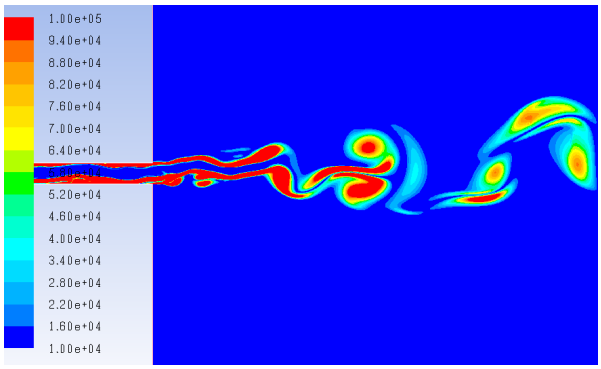

(0.015s)

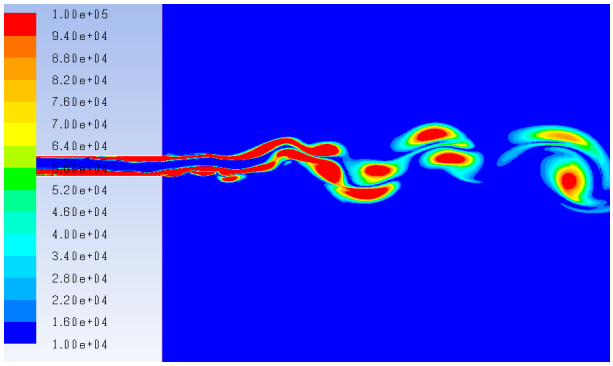

(0.02s)

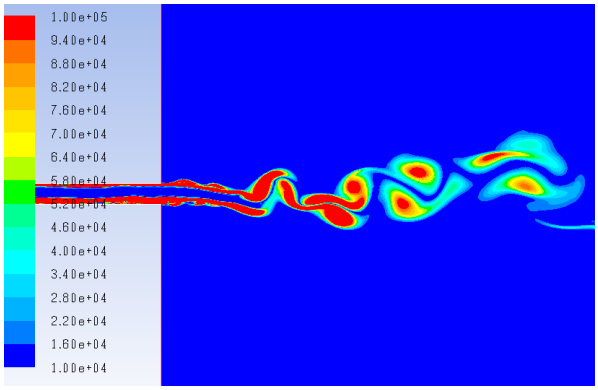

(0.025s)

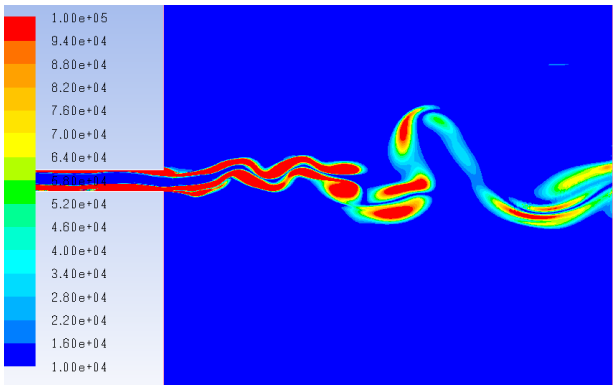

(0.03s)

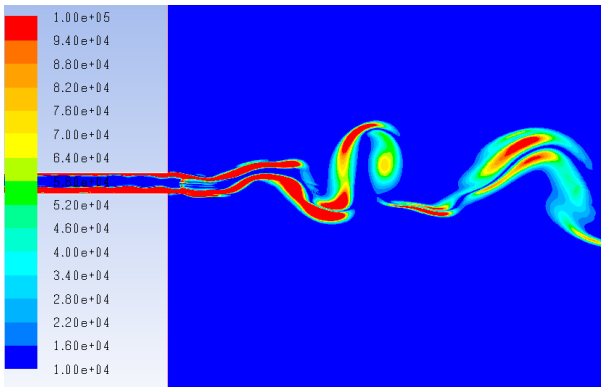

(0.035s)

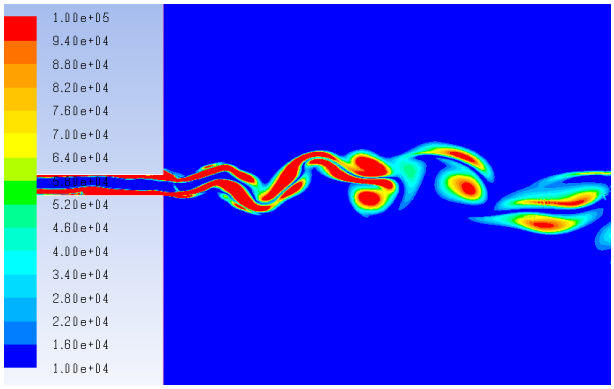

(0.04s)

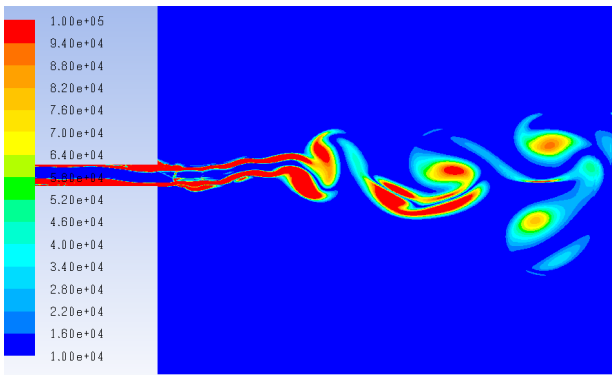

(0.045s)

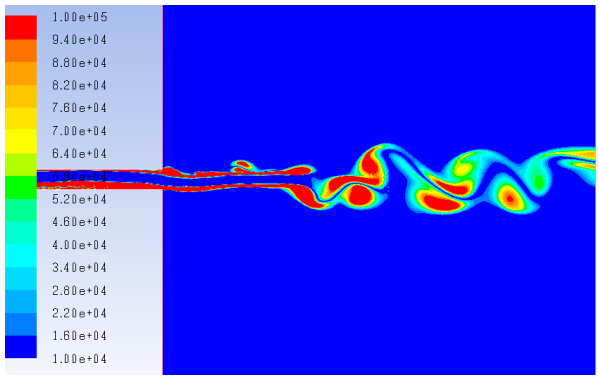

(0.05s)

Acknowledgement

The authors acknowledge the “Mésocentre de Calcul” at Université de Franche-Comté for the computation performed on the cluster “Lumière”.

References

[1] R.N. Raoelison, Coeval Cold Spray Additive Manufacturing Variances and Innovative Contributions, in: Cold-Spray Coat., Springer, Cham, 2018: pp. 57–94. doi:10.1007/978-3-319-67183-3_3.

[2] H. Assadi, H. Kreye, F. Gärtner, T. Klassen, Cold spraying – A materials perspective, Acta Mater. (n.d.). doi:10.1016/j.actamat.2016.06.034.

[3] A. Sova, S. Grigoriev, A. Okunkova, I. Smurov, Potential of cold gas dynamic spray as additive manufacturing technology, Int. J. Adv. Manuf. Technol. 69 (2013) 2269–2278. doi:10.1007/s00170-013-5166-8.

[4] S. Marx, A. Paul, A. Köhler, G. Hüttl, Cold Spraying: Innovative Layers for New Applications, J. Therm. Spray Technol. 15 (2006) 177–183. doi:10.1361/105996306X107977.

[5] A. Moridi, S.M. Hassani-Gangaraj, M. Guagliano, M. Dao, Cold spray coating: review of material systems and future perspectives, Surf. Eng. 30 (2014) 369–395.

[6] R.N. Raoelison, C. Verdy, H. Liao, Cold gas dynamic spray additive manufacturing today: Deposit possibilities, technological solutions and viable applications, Mater. Des. 133 (2017) 266–287. doi:10.1016/j.matdes.2017.07.067.

[7] R.N. Raoelison, Y. Xie, T. Sapanathan, M.P. Planche, R. Kromer, S. Costil, C. Langlade, Cold gas dynamic spray technology: A comprehensive review of processing conditions for various technological developments till to date, Addit. Manuf. 19 (2018) 134–159. doi:10.1016/j.addma.2017.07.001.

[8] S. Yin, M. Meyer, W. Li, H. Liao, R. Lupoi, Gas Flow, Particle Acceleration, and Heat Transfer in Cold Spray: A review, J. Therm. Spray Technol. 25 (2016) 874–896. doi:10.1007/s11666-016-0406-8.

[9] R.C. Dykhuizen, M.F. Smith, Gas Dynamic Principles of Cold Spray, J. Therm. Spray Technol. 7 (1998) 205–212. doi:10.1361/105996398770350945.

[10] H. Ye, Y. Yin, J. Wang, A One-Dimensional Flow Model with Adiabatic Friction for Rapid Estimation of Cold Spray Flow Conditions, J. Therm. Spray Technol. 24 (2015) 965–973. doi:10.1007/s11666-015-0279-2.

[11] M. Grujicic, C. Tong, W.S. DeRosset, D. Helfritch, Flow analysis and nozzle-shape optimization for the cold-gas dynamic-spray process, Proc. Inst. Mech. Eng. Part B J. Eng. Manuf. 217 (2003) 1603–1613. doi:10.1243/095440503771909980.

[12] H. Assadi, T. Schmidt, H. Richter, J.-O. Kliemann, K. Binder, F. Gärtner, T. Klassen, H. Kreye, On Parameter Selection in Cold Spraying, J. Therm. Spray Technol. 20 (2011) 1161–1176. doi:10.1007/s11666-011-9662-9.

[13] R.N. Raoelison, Analytical description of solid particles kinematics due to a fluid flow and application to the depiction of characteristic kinematics in cold spraying, Powder Technol. 319 (2017) 191–203. doi:10.1016/j.powtec.2017.06.029.

[14] X.-J. Ning, Q.-S. Wang, Z. Ma, H.-J. Kim, Numerical Study of In-flight Particle Parameters in Low-Pressure Cold Spray Process, J. Therm. Spray Technol. 19 (2010) 1211–1217. doi:10.1007/s11666-010-9548-2.

[15] J. Pattison, S. Celotto, A. Khan, W. O'Neill, Standoff distance and bow shock phenomena in the Cold Spray process, Surf. Coat. Technol. 202 (2008) 1443–1454. doi:10.1016/j.surfcoat.2007.06.065.

[16] X.-J. Ning, J.-H. Jang, H.-J. Kim, The effects of powder properties on in-flight particle velocity and deposition process during low pressure cold spray process, Appl. Surf. Sci. 253 (2007) 7449–7455. doi:10.1016/j.apsusc.2007.03.031.

[17] B. Samareh, O. Stier, V. Lüthen, A. Dolatabadi, Assessment of CFD Modeling via Flow Visualization in Cold Spray Process, J. Therm. Spray Technol. 18 (2009) 934–943. doi:10.1007/s11666-009-9363-9.

[18] H. Katanoda, T. Matsuoka, K. Matsuo, Experimental study on shock wave structures in constant-area passage of cold spray nozzle, J. Therm. Sci. 16 (2007) 40–45. doi:10.1007/s11630-007-0040-3.

[19] M.-W. Lee, J.-J. Park, D.-Y. Kim, S.S. Yoon, H.-Y. Kim, S.C. James, S. Chandra, T. Coyle, Numerical Studies on the Effects of Stagnation Pressure and Temperature on Supersonic Flow Characteristics in Cold Spray Applications, J. Therm. Spray Technol. 20 (2011) 1085–1097. doi:10.1007/s11666-011-9641-1.

[20] M.W. Lee, J.J. Park, D.Y. Kim, S.S. Yoon, H.Y. Kim, D.H. Kim, S.C. James, S. Chandra, T. Coyle, J.H. Ryu, W.H. Yoon, D.S. Park, Optimization of supersonic nozzle flow for titanium dioxide thin-film coating by aerosol deposition, J. Aerosol Sci. 42 (2011) 771–780. doi:10.1016/j.jaerosci.2011.07.006.

[21] R.N. Raoelison, E. Aubignat, M.-P. Planche, S. Costil, C. Langlade, H. Liao, Low pressure cold spraying under 6 bar pressure deposition: Exploration of high deposition efficiency solutions using a mathematical modelling, Surf. Coat. Technol. 302 (2016) 47–55. doi:10.1016/j.surfcoat.2016.05.068.

[22] Juha Lagerbom, Heli Koivuluoto, Jussi Larjo, Mikko Kylmälahti, Petri Vuoristo, Comparison of coatings prepared by two different cold spray processes, in: 2007.

[23] Y.T.R. Lee, H. Ashrafizadeh, G. Fisher, A. McDonald, Effect of type of reinforcing particles on the deposition efficiency and wear resistance of low-pressure cold-sprayed

metal matrix composite coatings, Surf. Coat. Technol. 324 (2017) 190–200. doi:10.1016/j.surfcoat.2017.05.057.

[24] M. Kulmala, P. Vuoristo, Influence of process conditions in laser-assisted low-pressure cold spraying, Surf. Coat. Technol. 202 (2008) 4503–4508. doi:10.1016/j.surfcoat.2008.04.034.

[25] G. Huang, H. Wang, X. Li, L. Xing, J. Zhou, Deposition efficiency of low pressure cold sprayed aluminum coating, Mater. Manuf. Process. 0 (2017) 1–7. doi:10.1080/10426914.2017.1415443.

[26] J. Morère, D.P. Schmidt, P. Liebersbach, J.J. Watkins, Suppression of Clogging in Cold Spray Nozzles, (2018).

[27] M. Siopis, Study of Nozzle Clogging During Cold Spray, (2017).

[28] X. Wang, B. Zhang, J. Lv, S. Yin, Investigation on the Clogging Behavior and Additional Wall Cooling for the Axial-Injection Cold Spray Nozzle, J. Therm. Spray Technol. 24 (2015) 696–701. doi:10.1007/s11666-015-0227-1.

[29] Q. Blochet, F. Delloro, F. N'Guyen, F. Borit, M. Jeandin, K. Roche, G. Surdon, Influence of spray angle on cold spray with Al for the repair of aircraft components, in: ITSC 2014, DVS, Barcelone, Spain, 2014: pp. 69–74. https://hal.archives-ouvertes.fr/hal-01055104 (accessed February 25, 2019).

[30] D.L. Gilmore, R.C. Dykhuizen, R.A. Neiser, T.J. Roemer, M.F. Smith, Particle Velocity and Deposition Efficiency in the Cold Spray Process, J. Therm. Spray Technol. 8 (1999) 576–582. doi:10.1361/105996399770350278.

Figures and tables (excluding the figures of the section Appendix)

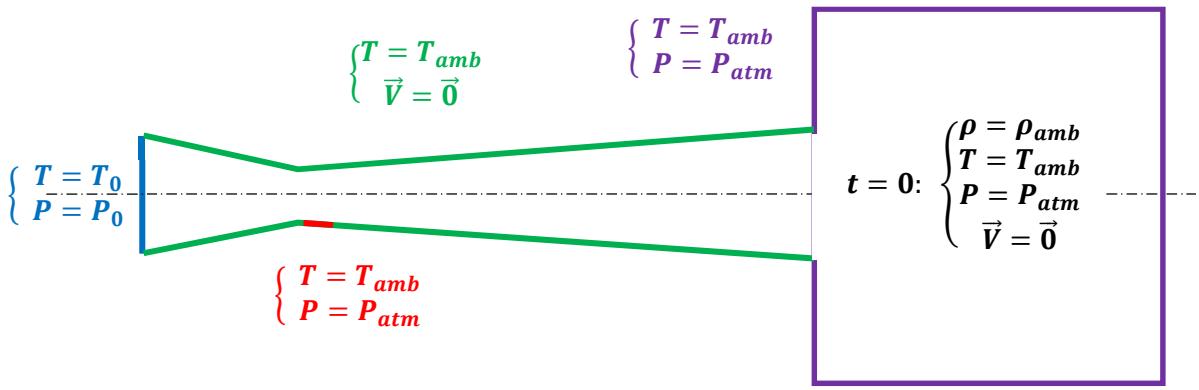

Fig.1. The 2D geometrical model with both boundary conditions and initial conditions.

Computation performance			Space-time discretization			Computation duration and storage		
RAM	Core	Speed	Nodes	Δt	Total time	CPU time	Backup time	Storage
144GB	96	66.33 Tflops	823901	1µs	0.05s	36Hrs14min	every 1ms	24.8GB

Table 1. Computational details with the performance allocated by the Cluster Lumière of “Mésocentre de Calcul de Franche-Comté”.

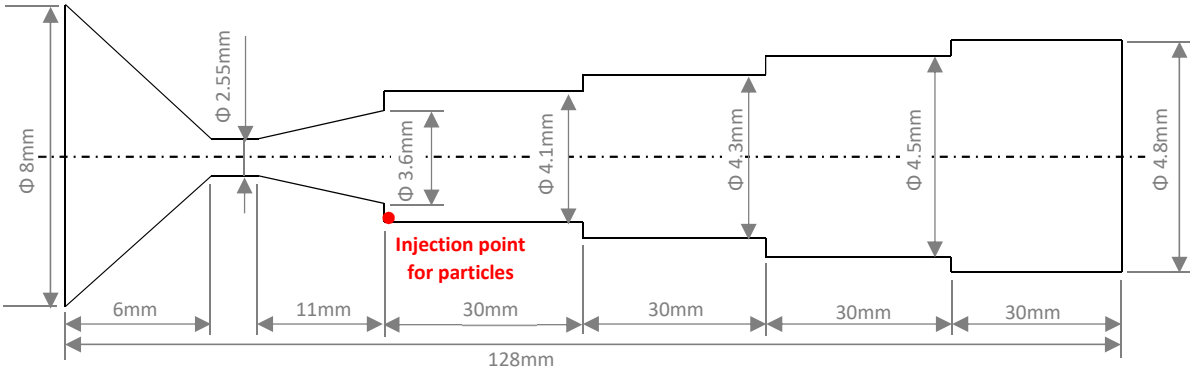

Fig. 2. Specification of the nozzle shape and dimension with the radial powder injection location.

Powder	Size range	d10	d50	d90
Cu	5-112µm	30.54µm	50.14µm	79.29µm

Table 2. Granulometry details of the powder feedstock.

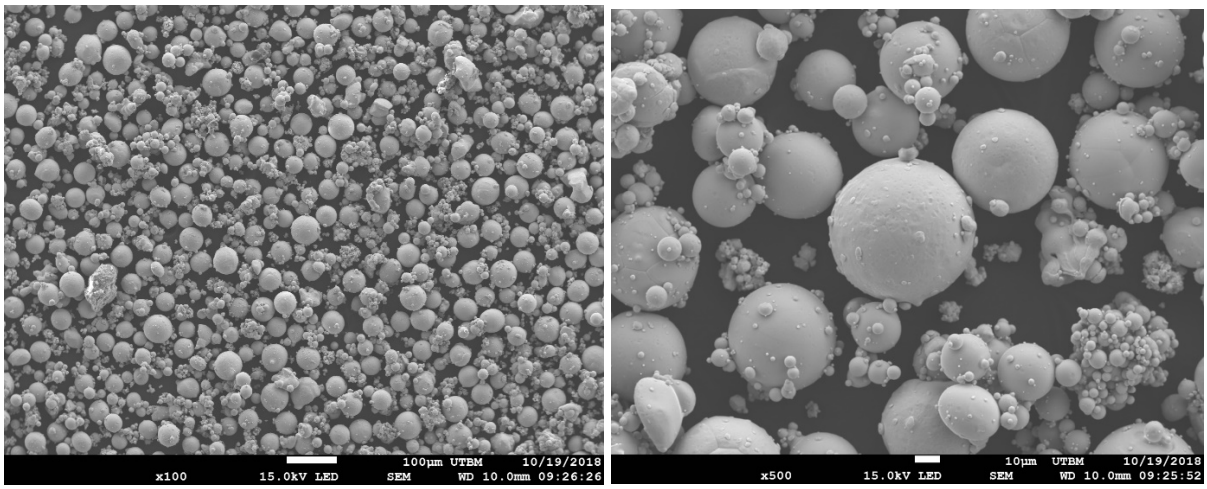

Fig. 3. SEM observations of the powder feedstock.

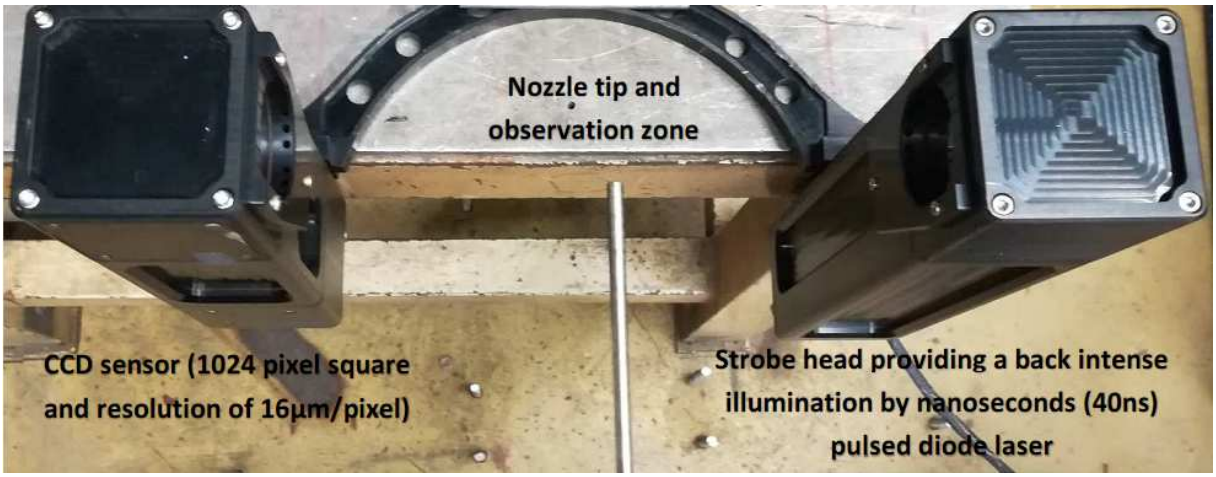

(a)

(b)

Fig. 4. Shadowgraph system (SprayCam) and mounting for observing the particles motion: top view (a) and front view (b).

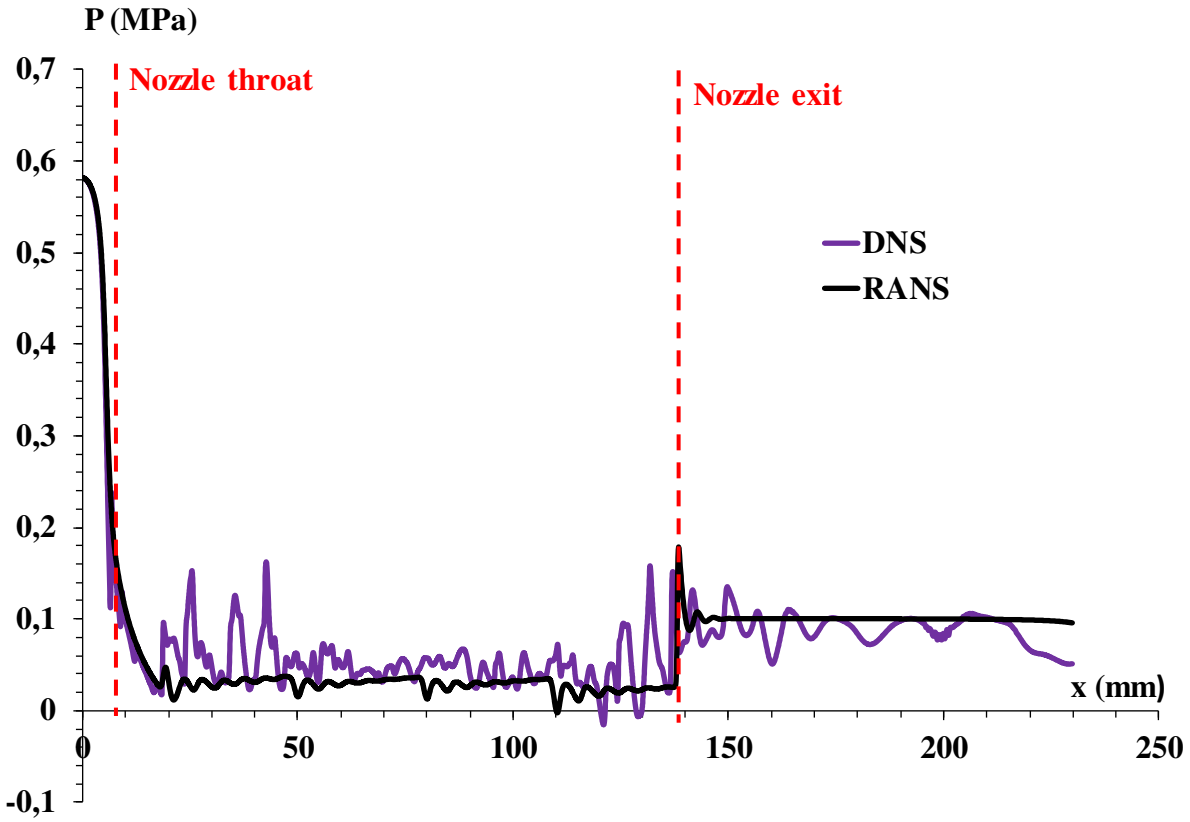

Fig. 5. Centerline distribution of the expanding gas pressure: regular fluctuation of a RANS computation compared to a random fluctuation of a DNS computation (captured at the time t=0.01s).

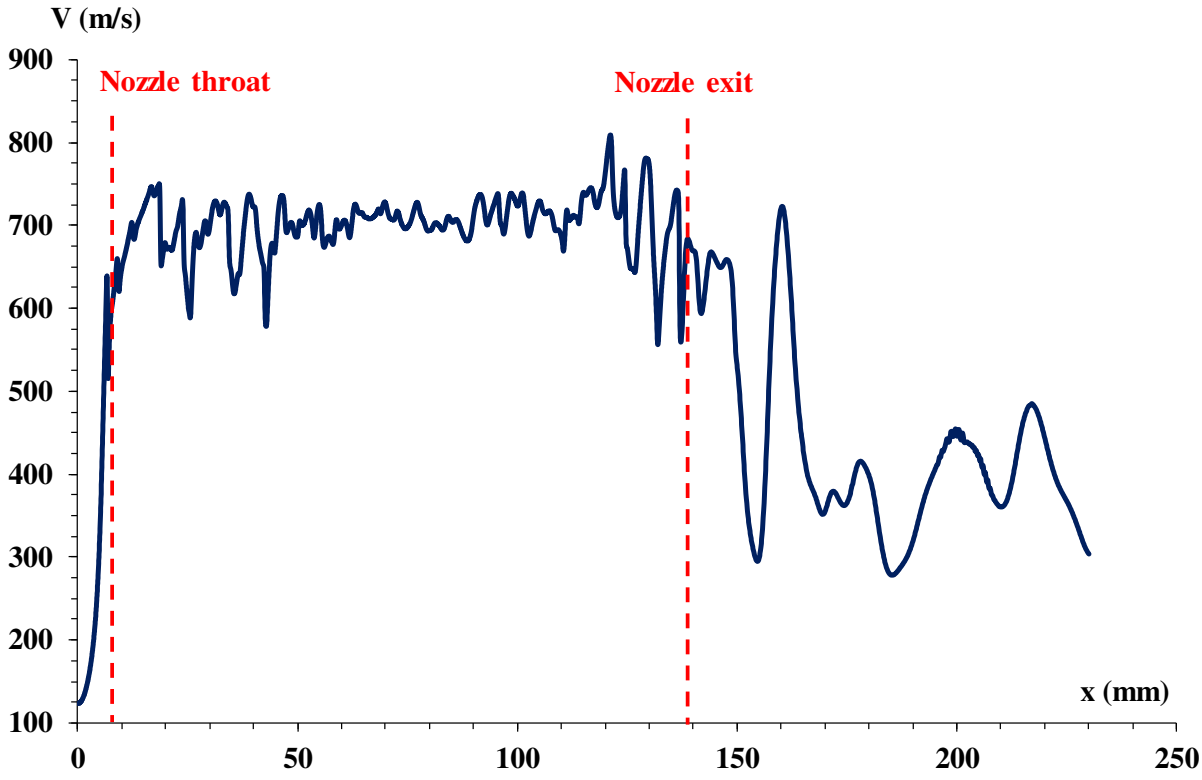

(a)

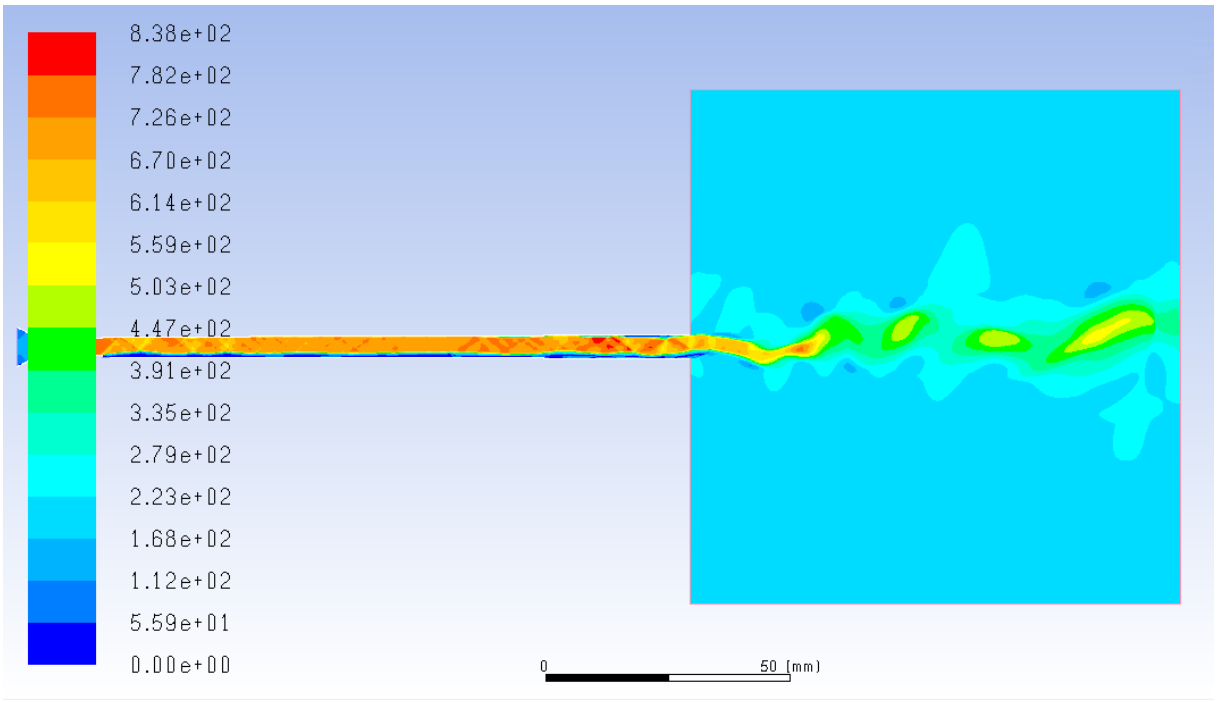

(b)

Fig. 6. Turbulence of the flow captured at the time t=0.01s: (a) centerline distribution of the velocity magnitude revealing the turbulence of the flow, (b) isovalues of velocity magnitude in m/s showing the irregular oscillation of the flow due to the turbulence.

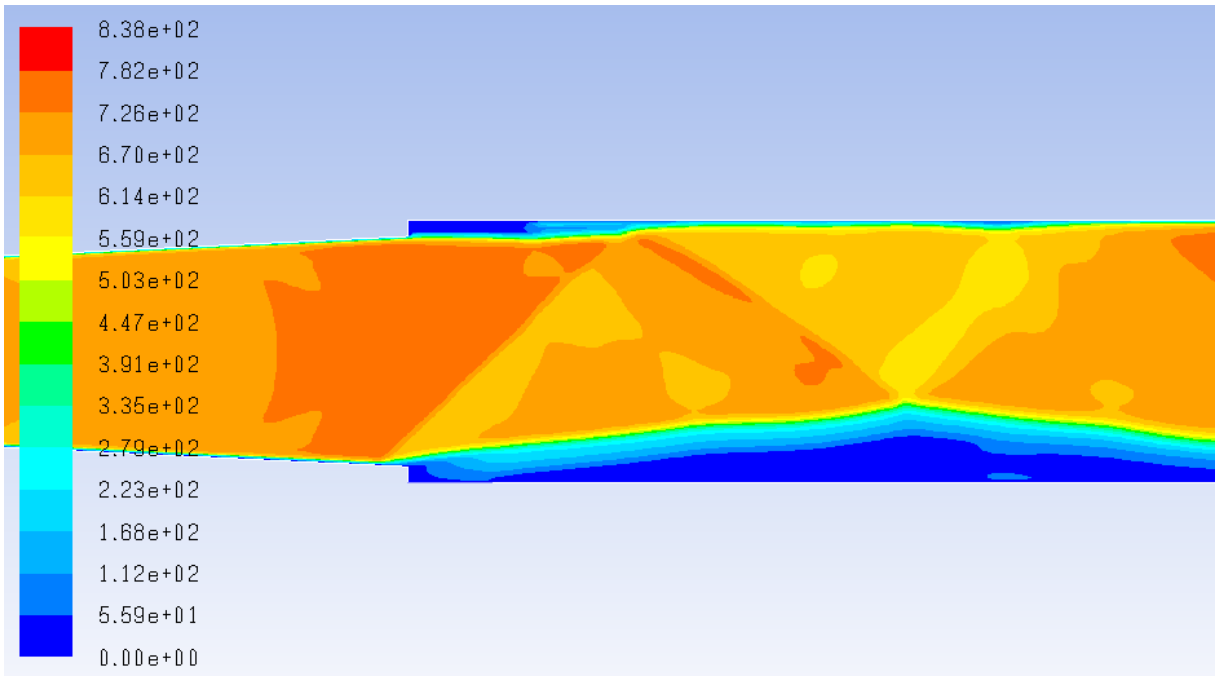

(a)

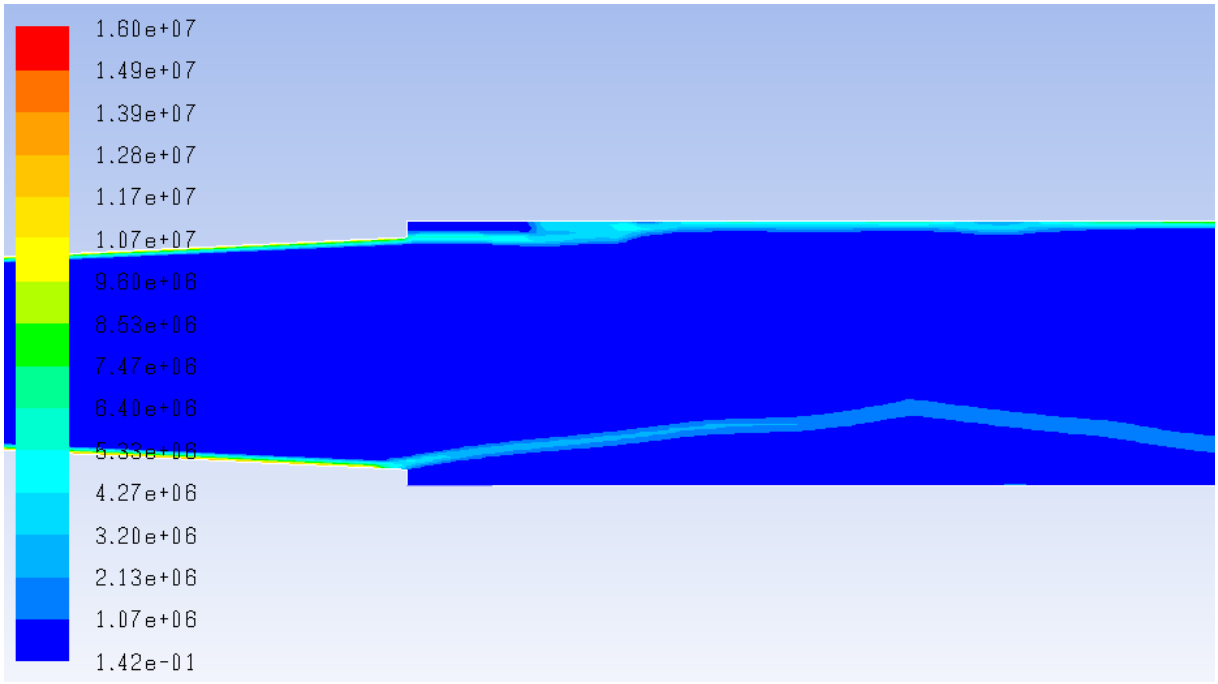

(b)

Fig. 7. Deformation of the supersonic jet at inside the nozzle due to the secondary gas at the zone of particle feeding, and then onset of oscillatory stream in the flow direction as shown by the gas stream velocity in m/s (a) and the rate of rotation in s^{-1} (b).

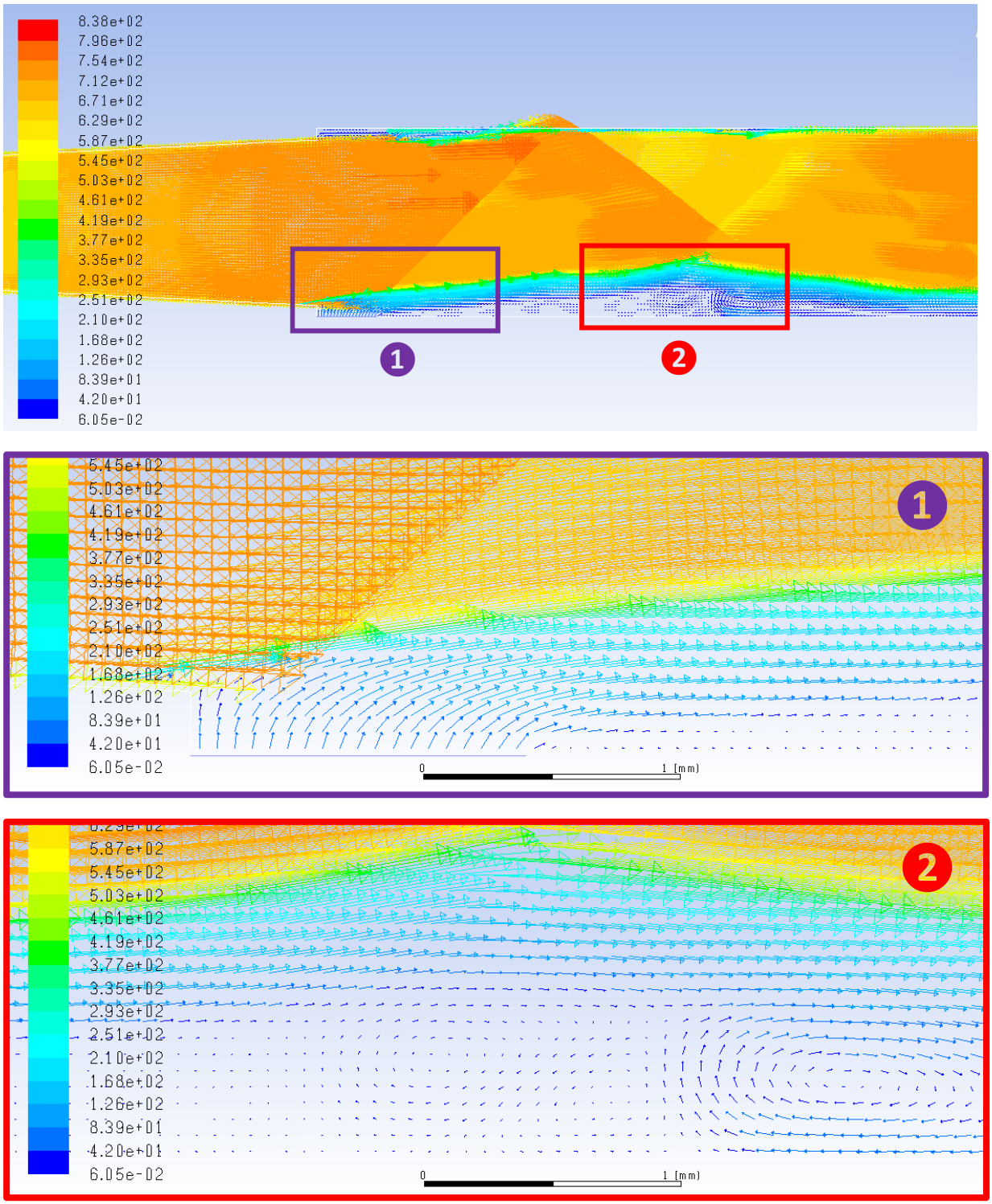

Fig. 8. Gas stream velocity (in m/s) at the zone of secondary gas inlet and development of parietal swirls due to the shearing jet.

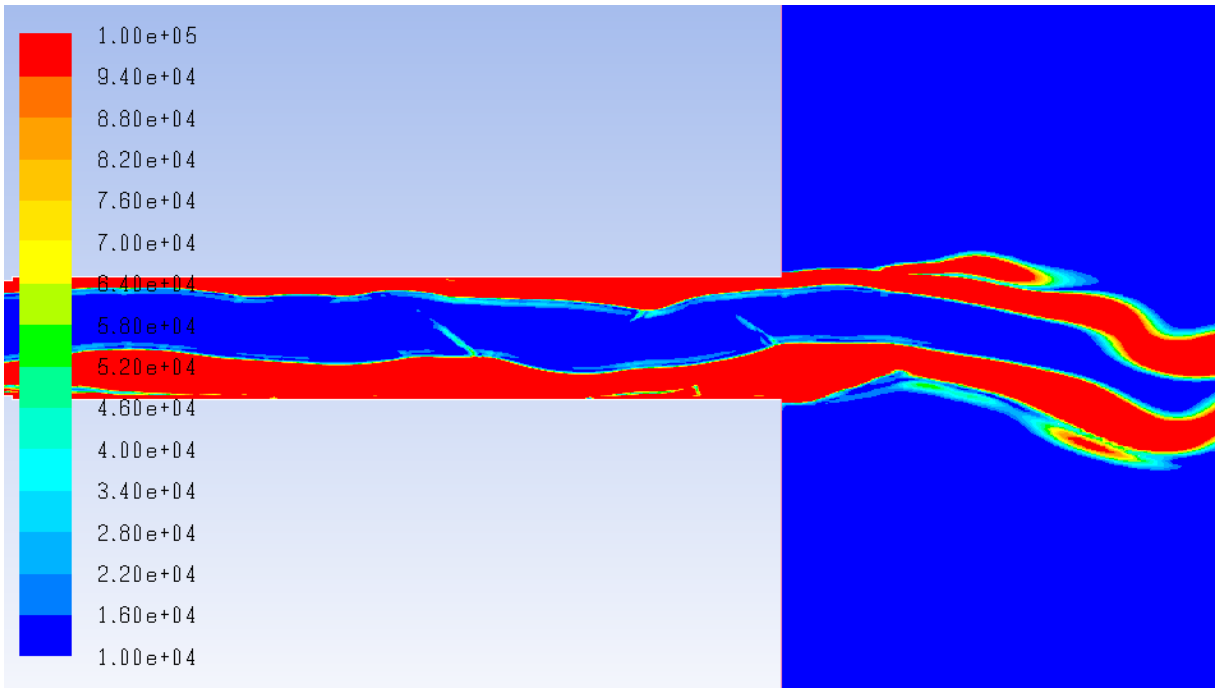

Fig. 9. Rate of rotation (s^{-1}) within the shear layers due to the shearing flow that shows the jet deformation inside the nozzle, across the exit section, and then outside.

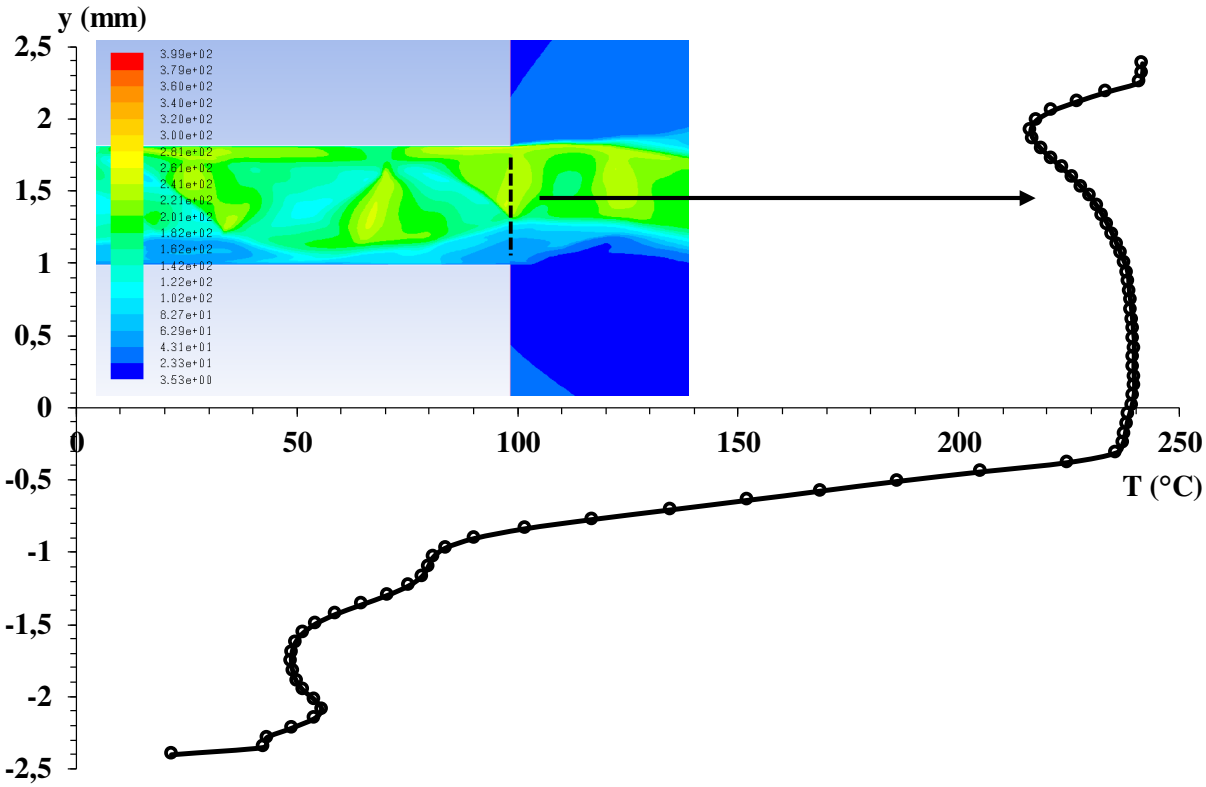

(a)

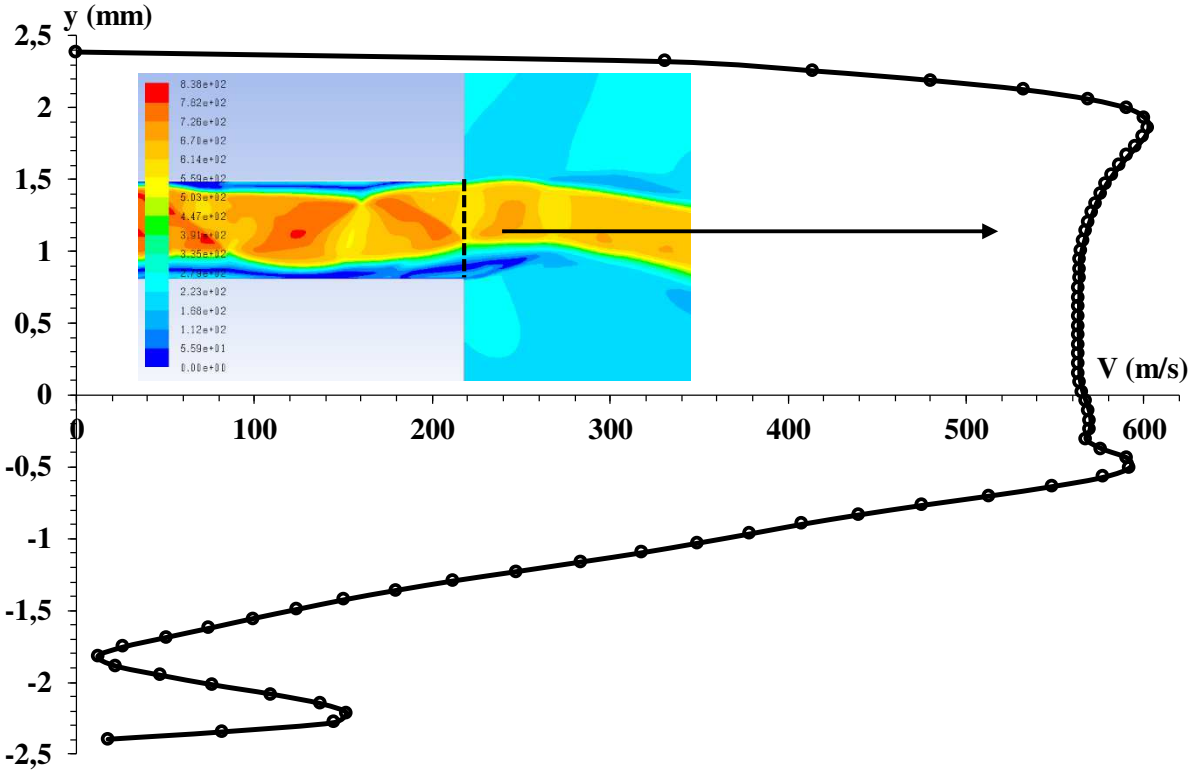

(b)

Fig. 10. Radial distribution of temperature (a) and velocity (b) across the nozzle exit that show thermal and kinematic confinement near the upper wall.

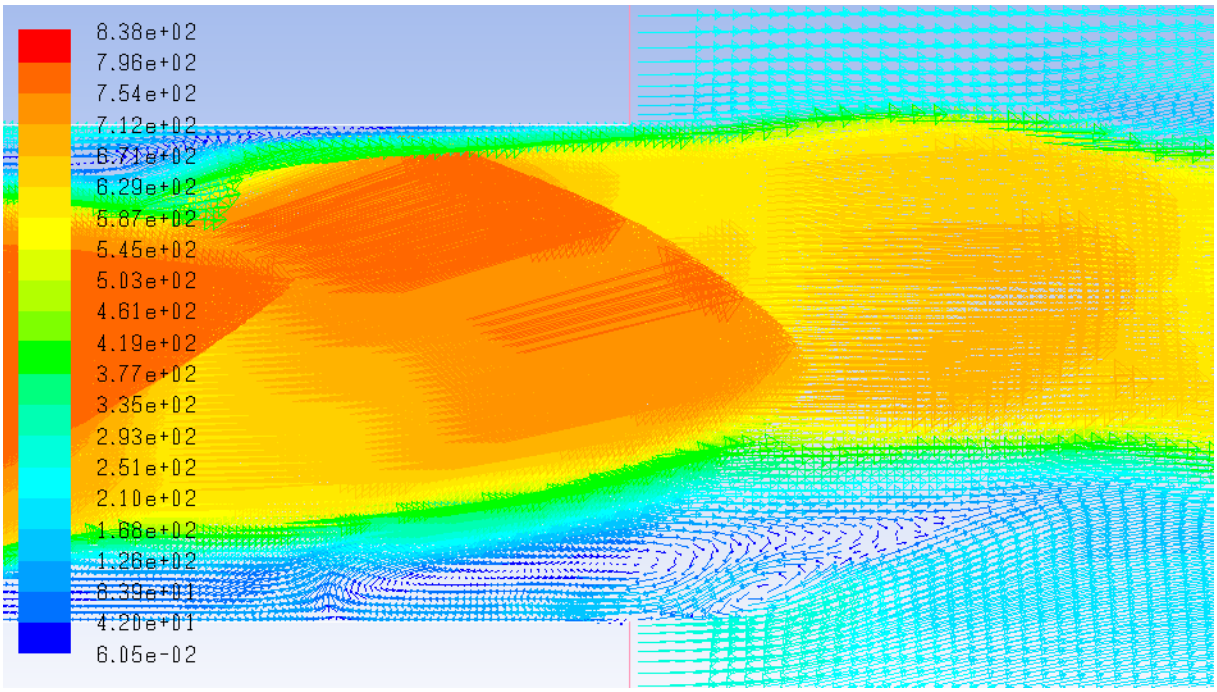

Fig. 11. Development of swirls at the nozzle exit due the jet shearing, and subsequent flow deviation (t=0.01s).

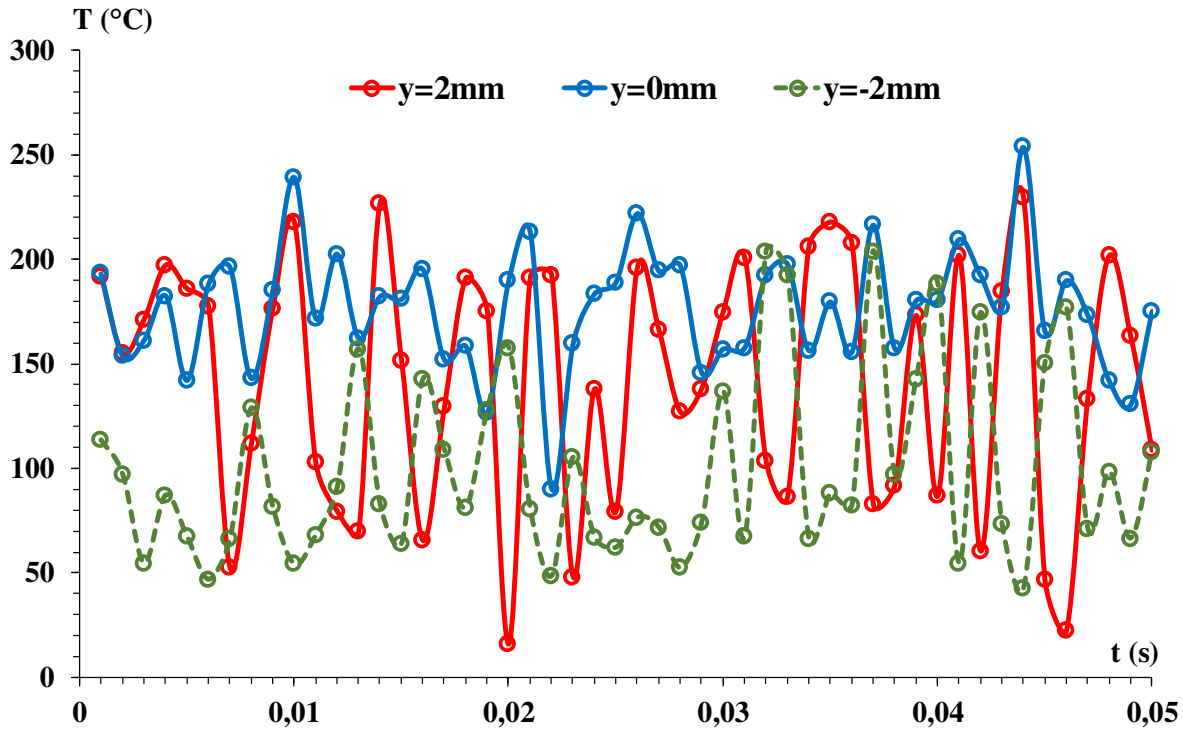

(a)

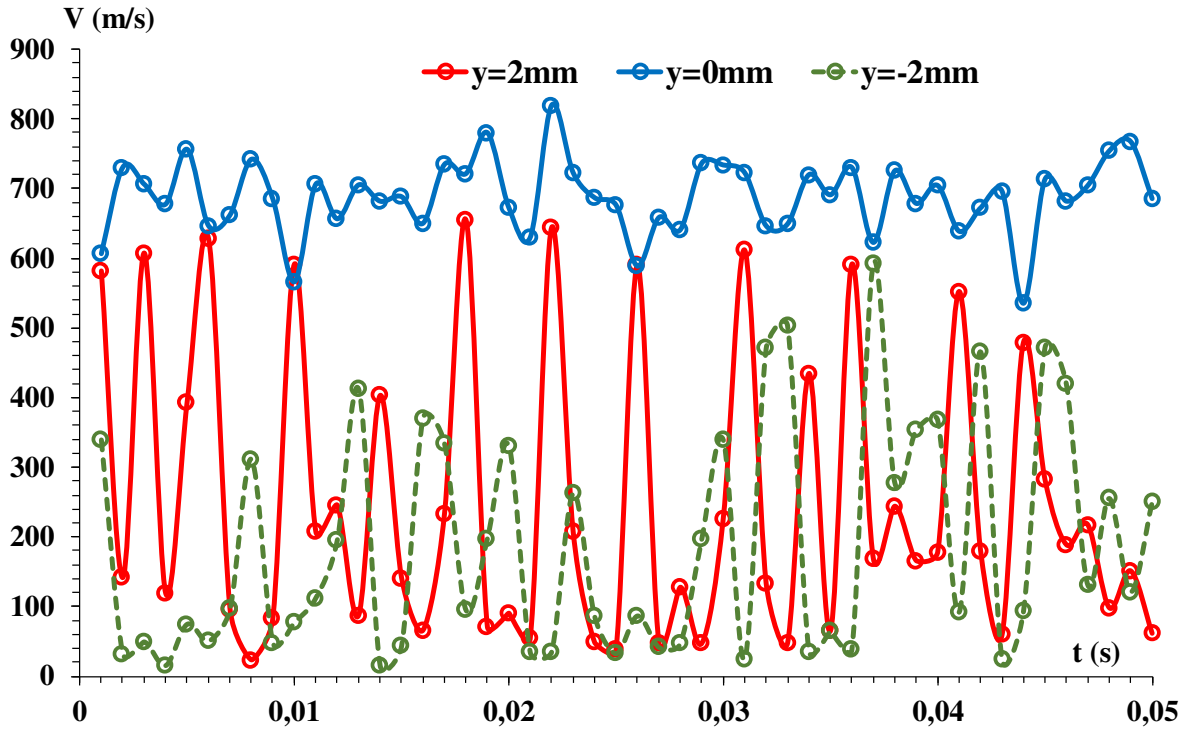

(b)

Fig. 12. Repetitive peaks of temperature (a) and velocity (b) at the top region of the nozzle exit.

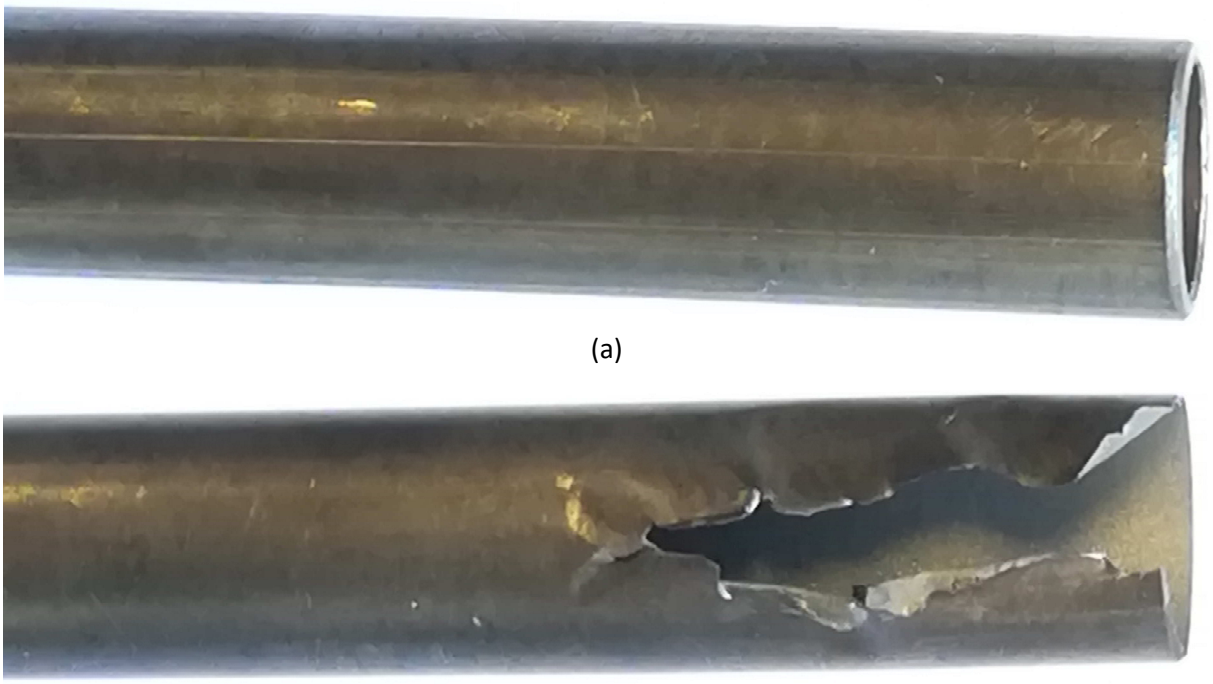

(a)

(b)

Fig. 13. Comparison between an unused nozzle and a worn nozzle: pristine tip (a) and eroded tip (b).

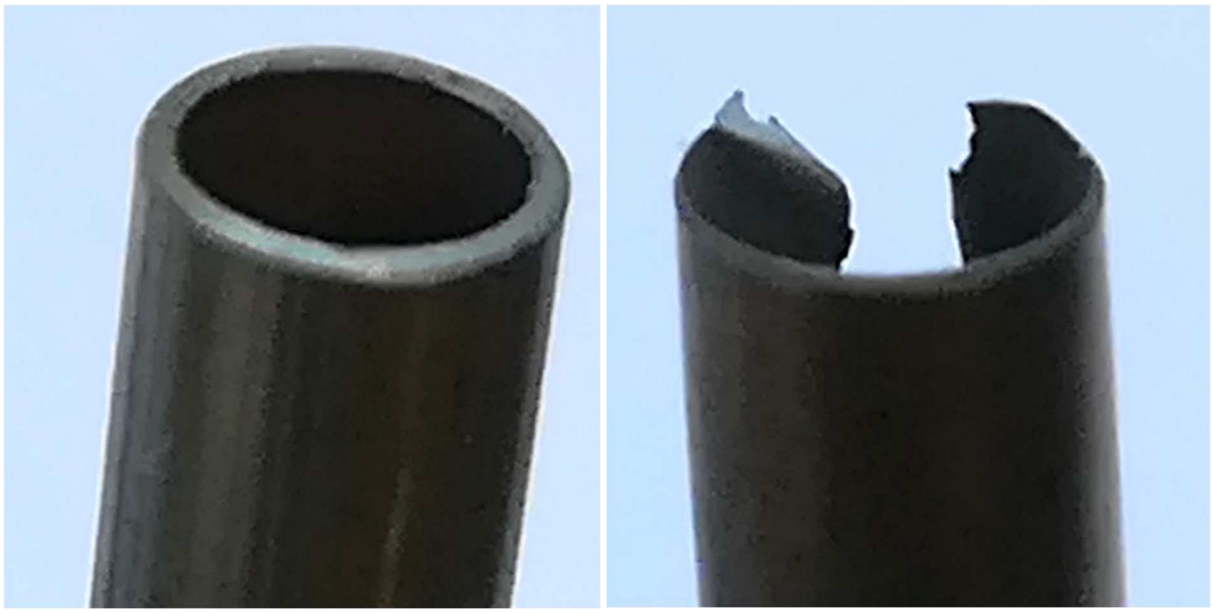

(a) (b)

Fig. 14. Comparison between an unused nozzle and a thinned nozzle: pristine tip (a) and eroded tip (b).

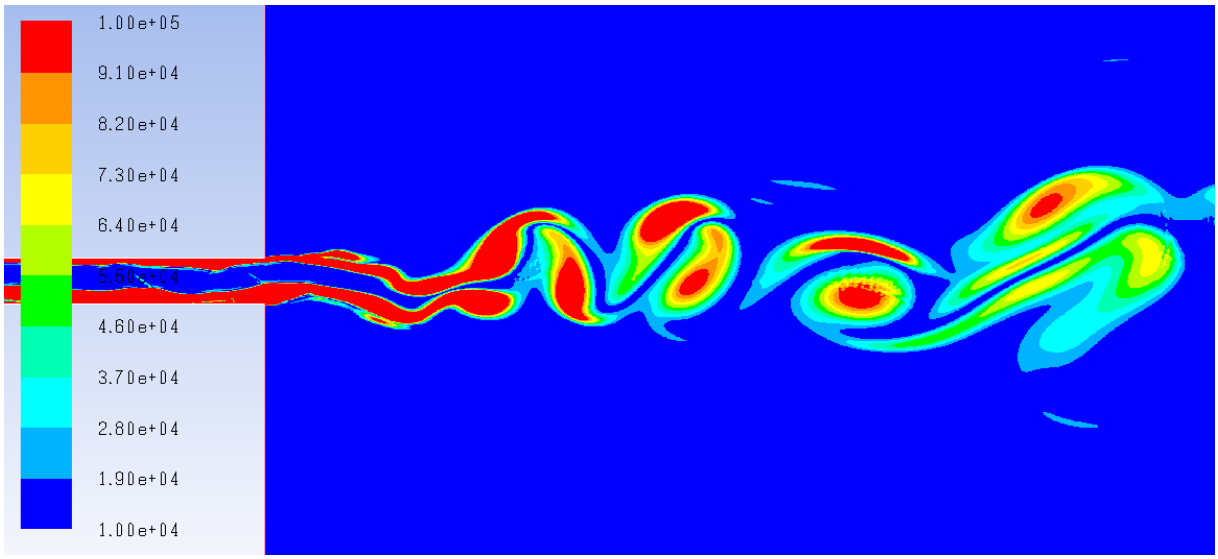

(a)

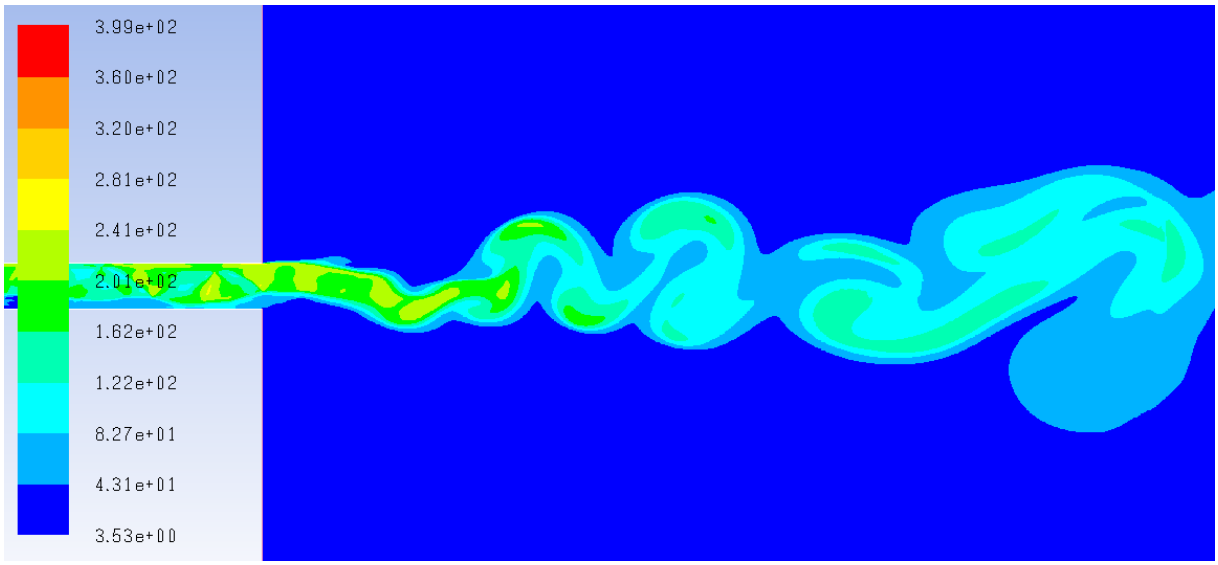

(b)

Fig. 15. Virtual visualization of the flow regimes: a shearing jet while leaving the nozzle and entering the atmospheric media, and then a strongly oscillatory regime revealed by both vorticity shedding (a) and thermal turbulent plume (b) confined along the flow pattern.

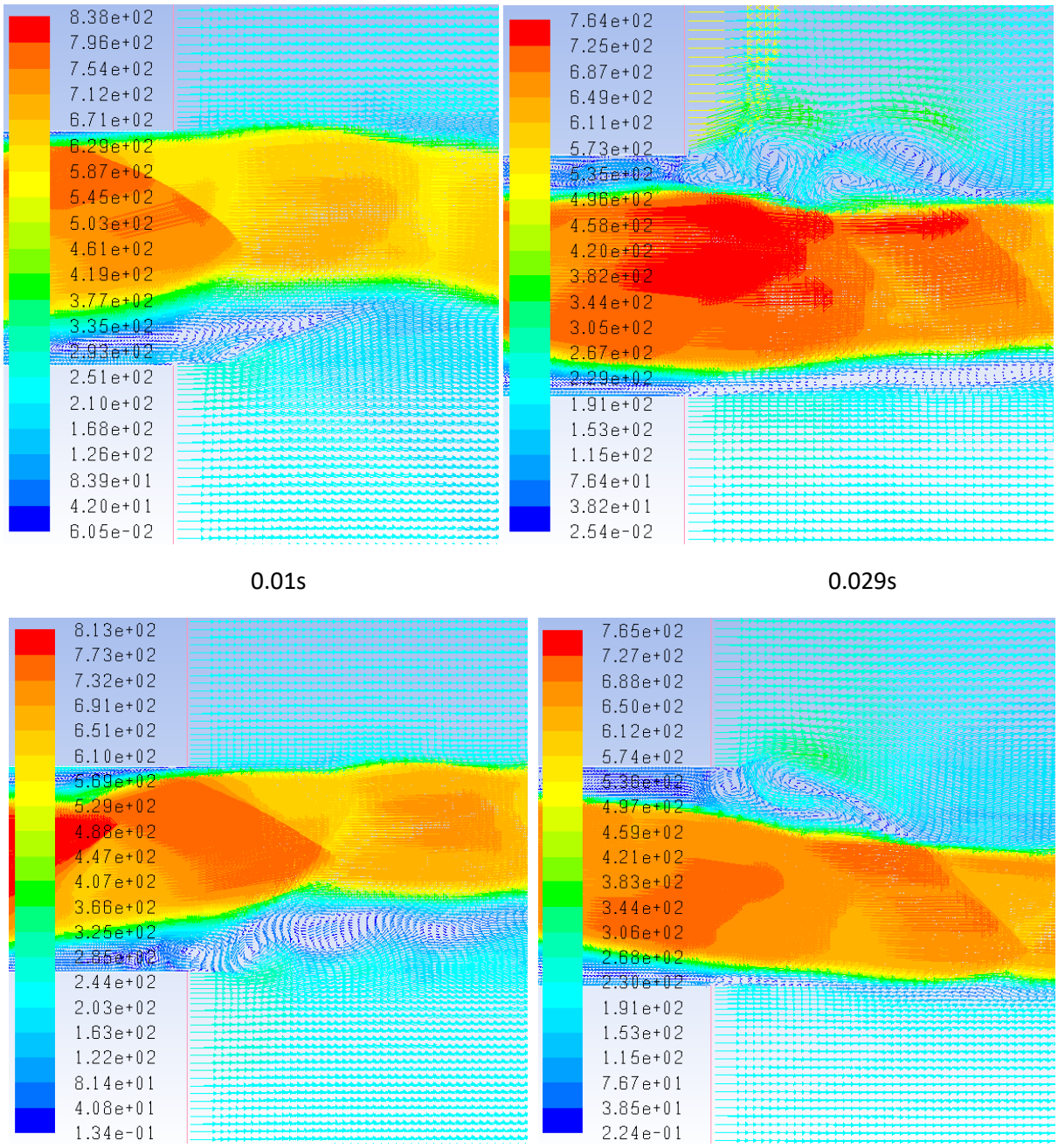

Fig. 16. Instable swirls at the sheared layers region, on top and then on bottom and vice-versa alternately at sporadic time intervals.

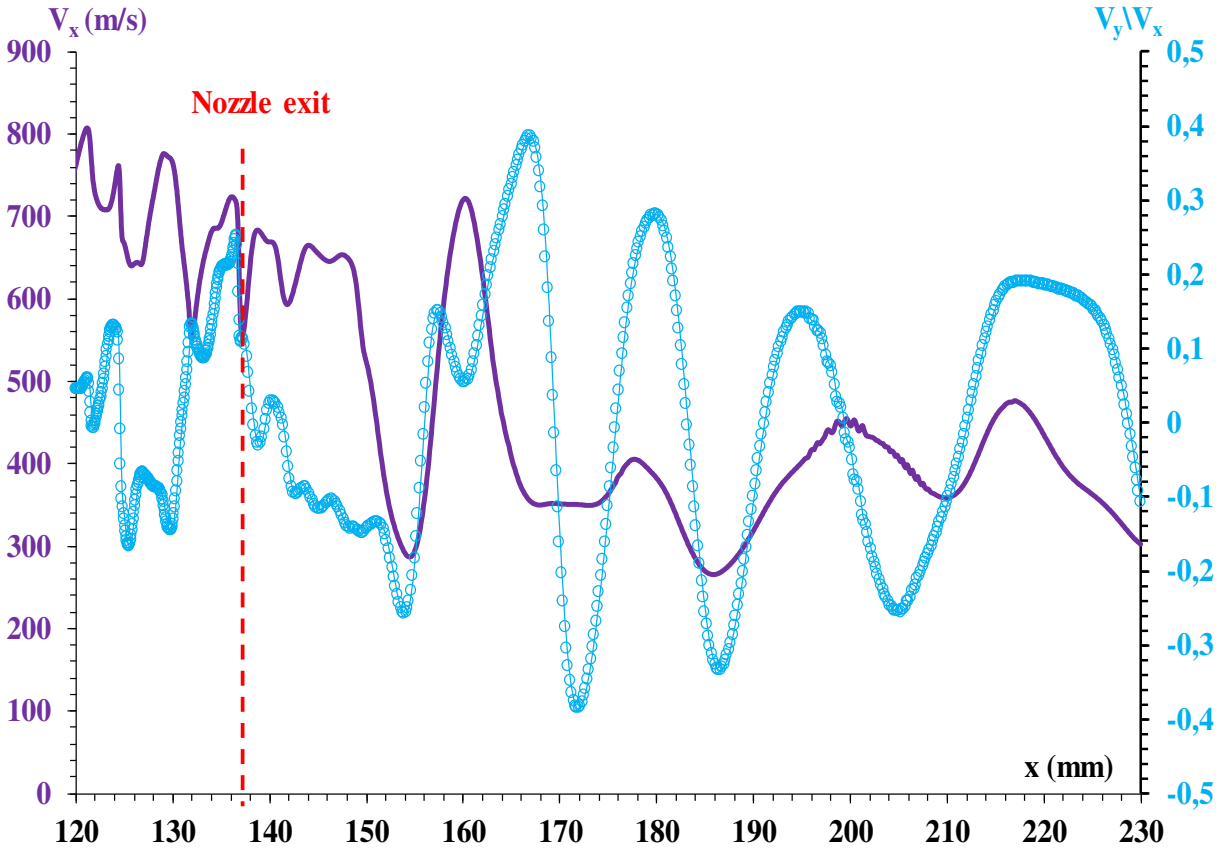

Fig. 17. Vy\Vx ratio distribution that shows the instability growing along the flow direction due to the fluctuation in Vy, and predominance of Vx that drives the gas stream (t=0.01s).

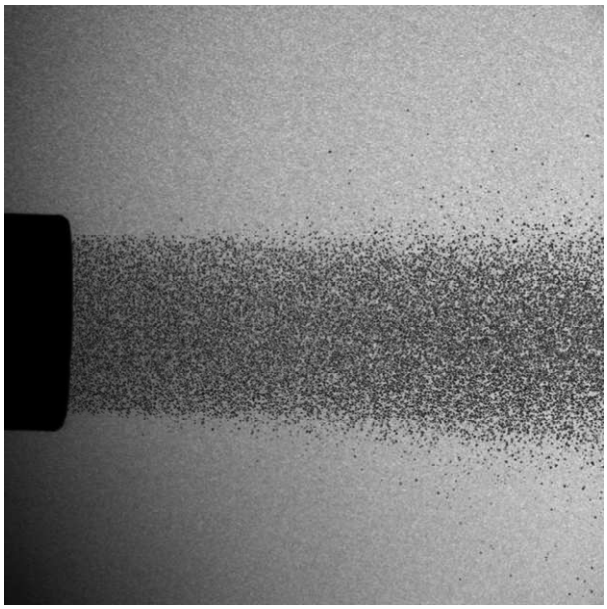

(a): 135mm<x<150mm

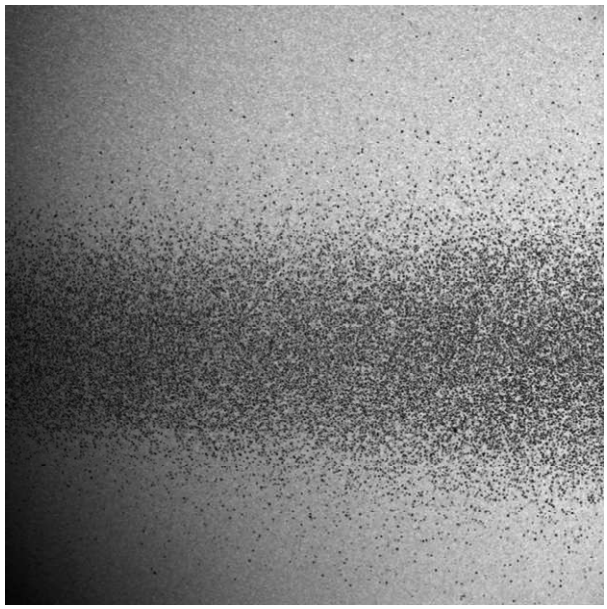

(b): 150mm<x<165mm

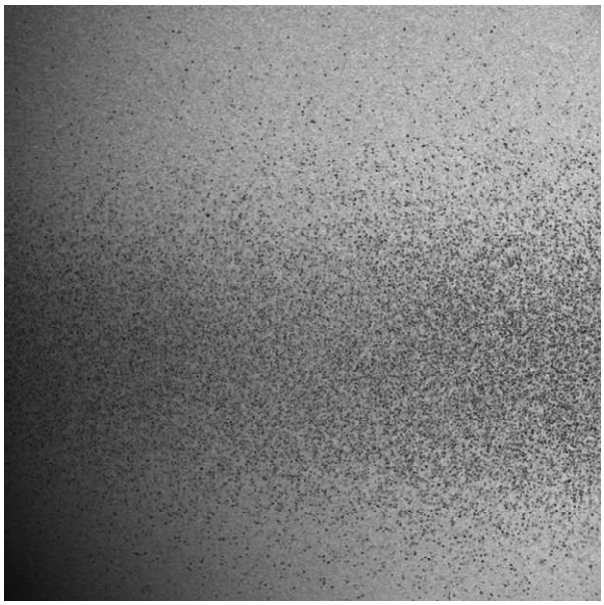

(c): 165mm<x<180mm

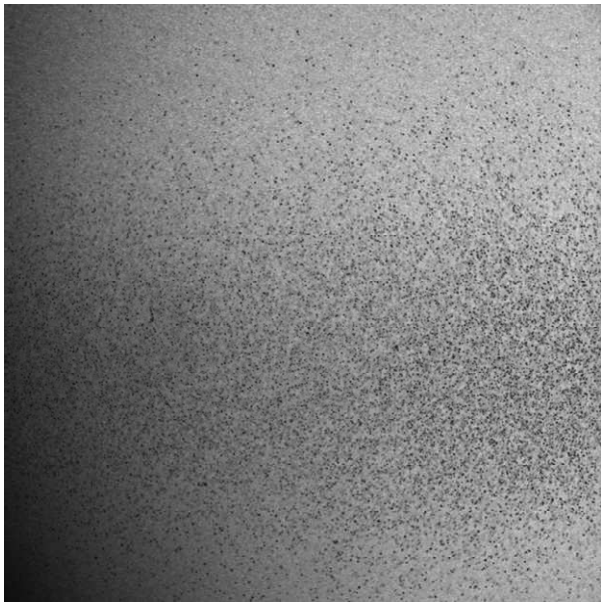

(d): 180mm<x<195mm

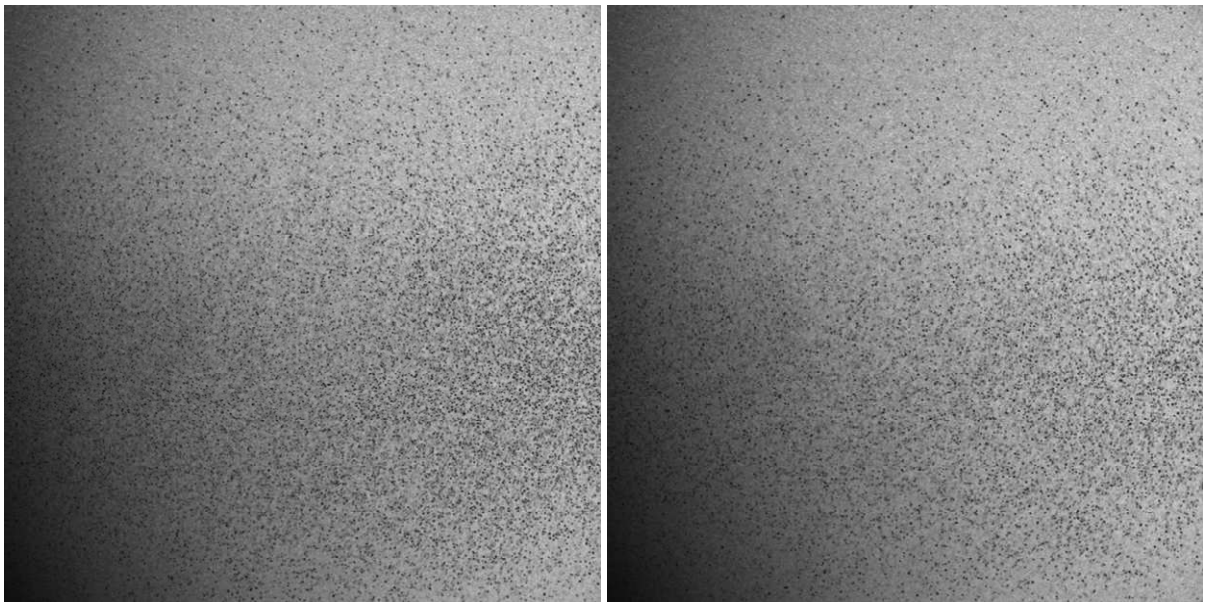

(e): 195mm<x<210mm (f): 210mm<x<225mm

Fig. 18. Regimes of particles flow that follows the gas behavior: nearly uniform straight jet where the gas stream is less deformed (a), onset of particles deviation due to the self-oscillated gas flow (b), and particles dispersion where the gas flow develops wakes (c-e).

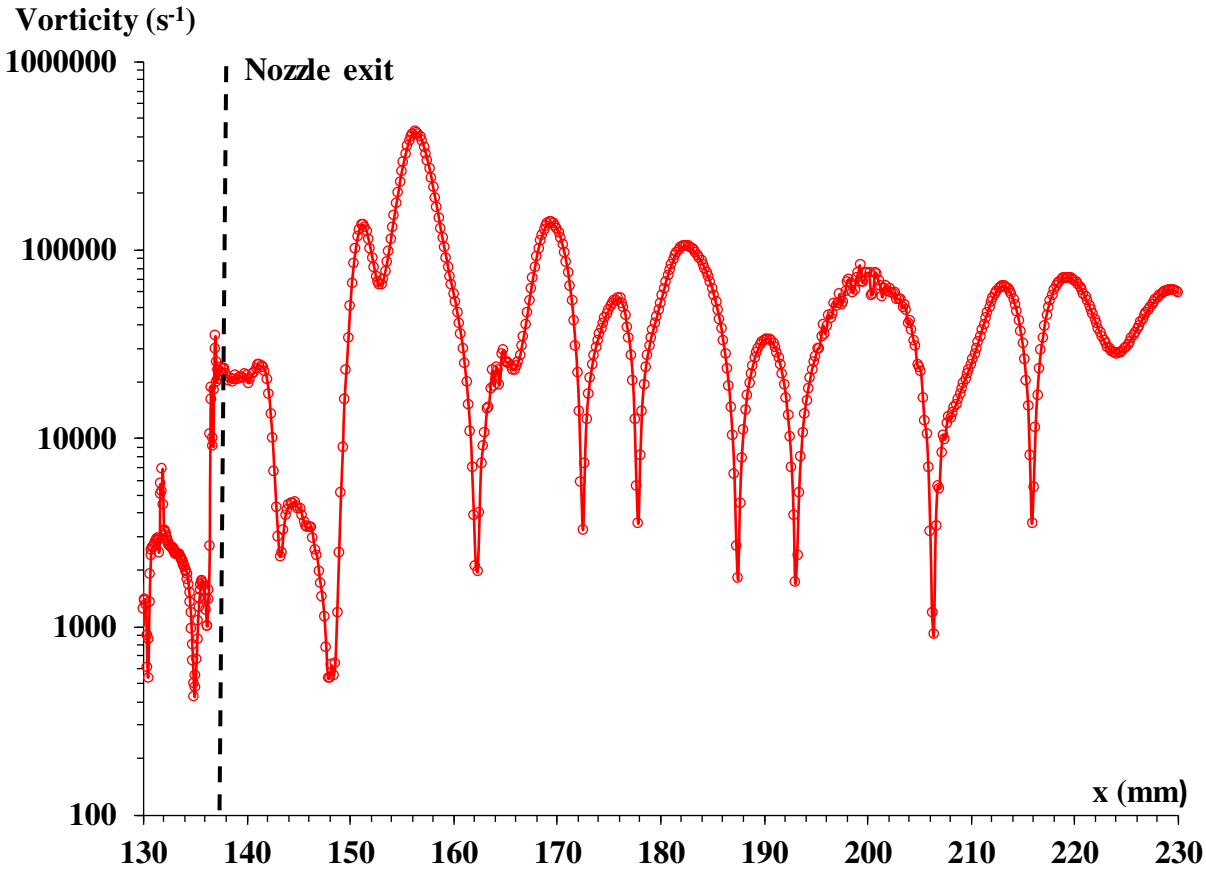

Fig. 19. Vorticity shedding magnitude distribution (t=0.01s) along the centerline where the zone of high vorticity beyond 150mm specifies the vortex shedding and corresponds to the experimental transition of particles dispersion.